Actin dynamics drive cell-like membrane deformation

Camille Simon, Remy Kusters, Valentina Caorsi, Antoine Allard, Majdouline Abou-Ghali, John Manzi, Aurélie Di Cicco, Daniel Lévy, Martin Lenz, Jean-François Joanny, et al.

Title: Actin dynamics drive cell-like membrane deformation.

Camille Simon[†1,2], Rémy Kusters[†1,2], Valentina Caorsi[†1,2], Antoine Allard[1,2,3], Majdouline Abou-Ghali[1,2], John Manzi[1,2], Aurélie Di Cicco[1,2], Daniel Lévy[1,2], Martin Lenz[4], Jean-François Joanny[1,2,5], Clément Campillo[3], Julie Plastino[1,2], Pierre Sens[1,2&], Cécile Sykes[1,2&]

[†]These authors contributed equally to this work.

[&]These authors contributed equally to this work.

Abstract: Cell membrane deformations are crucial for proper cell function. Specialized protein assemblies initiate inward or outward membrane deformations that the cell uses respectively to uptake external substances or probe the environment. The assembly and dynamics of the actin cytoskeleton are involved in this process, although their detailed role remains controversial. We show here that a dynamic, branched actin network is sufficient to initiate both inward and outward membrane deformation. The polymerization of a dense actin network at the membrane of liposomes produces inward membrane bending at low tension, while outward deformations are robustly generated regardless of tension. Our results shed light on the mechanism cells use to internalize material, both in mammalian cells, where actin polymerization forces are required when membrane tension is increased, and in yeast, where those forces are necessary to overcome the opposing turgor pressure. By combining experimental observations with physical modeling, we propose a mechanism that explains how membrane tension and the architecture of the actin network regulate cell-like membrane deformations.

[1] Laboratoire Physico Chimie Curie, Institut Curie, PSL Research University, CNRS UMR168, 75005, Paris, France. [2] Sorbonne Universités, UPMC Univ Paris 06, 75005, Paris, France. [3] LAMBE, Université Evry, CNRS, CEA, Université Paris-Saclay, Evry F-91025, France. [4] LPTMS, CNRS, Univ. Paris-Sud, Université Paris-Saclay, 91405 Orsay, France. [5] ESPCI-Paris, 10 rue Vauquelin, 75005, Paris, France.

Many cell functions rely on the ability of cells to change their shape. The deformation of the cell membrane is produced by the activity of various proteins that curve the membrane inwards or outwards, by exerting pulling and pushing forces or by imposing membrane curvature via structural effects. When cells take up external material, it is often associated with membrane invaginations followed by vesicle transport. This process is called endocytosis. Such inward deformation of the cell membrane can be initiated by specific proteins, such as clathrin, which coat the membrane and impose geometrical constraints that bend the membrane inwards. In this view, the action of the actin cytoskeleton, a filamentous network that forms at the membrane, is crucial only at a later stage for membrane elongation. Nevertheless, impressive correlation methods revealed unambiguously that, in yeast, membrane bending is not triggered by the presence of coat proteins, but by a dynamic actin network formed at the membrane through the Arp2/3 complex branching agent [1, 2, 3]. In mammalian cells, clathrin-mediated endocytosis requires the involvement of actin if the plasma membrane is tense, *e.g.* following osmotic swelling or mechanical stretching [4]. However, the exact mechanism of membrane deformation in this process is still poorly understood. Strikingly, the same type of branched actin network is able to bend the membrane the other way in, outward-pointing membrane deformations, called dendritic filopodia. These structures are precursors of dendritic spines in neurons, and essential for signal transmission [5]. Dendritic filopodia differ from conventional filopodia, localized at the leading edge of the cell, where actin filaments are parallel. Whereas the pioneering work of Liu et al[6] already established how thin filopodia form by bundling actin filaments, the production of a dendritic filopodia-like membrane protrusion containing a branched actin network has never been investigated.

How the same branched actin structure can be responsible for the initiation of filopodia, which are outward-pointing membrane deformations, as well as endocytic invaginations that deform the membrane inward, is what we want to address in this paper. Such a question is difficult to investigate in cells that contain redundant mechanisms for cell deformation. Actin dynamics triggered at a liposome membrane provide a control on experimental parameters such as membrane composition, curvature and tension, and allow the specific role of actin dynamics to be addressed. We unambiguously show that the same branched actin network is able to produce both endocytosis-like and dendritic filopodia-like deformations. With a theoretical model, we predict under which conditions the stress exerted on the membrane will lead to inward and/or outward pointing membrane deformations. Combining experiments and theory allows us to decipher how the interplay between membrane tension, actin dynamics, and actin network structure produces inward or outward membrane deformations.

Membrane deformations: tubes and spikes

Liposomes are covered with an activator of the Arp2/3 complex, pVCA, the proline rich domain-verprolin homology-central-acidic sequence from human WASP, which is purified with a streptavidin tag, and that we call hereafter S-pVCA. A branched actin network grows at their surface when placed in a mixture containing monomeric actin, profilin, the Arp2/3 complex and capping protein (CP) ("reference condition", Methods and Fig. 1a). Strikingly, the membrane of liposomes is not smooth, but instead displays a rugged profile: membrane tubes, hereafter called "tubes", radiate from the liposome surface and extend into the actin network (Fig. 1b), even when comet formation has occurred [7, 8] (Supplementary Fig. 1a). The initiation of these tubes is reminiscent of early stage of endocytosis. Interestingly, some liposomes display another type of membrane deformation, characterized by a conical shape, hereafter referred to as "spikes" that points towards the liposome interior (Fig. 1b), and are

reminiscent of dendritic filopodia structures in cells. Some of the liposomes carry both tubes and spikes, while others are "undetermined", as no membrane deformation is visually detectable (Fig. 1b). Spikes have a wide base of a few microns and a length that spans at least half of the liposome diameter. In contrast, tubes are thin, with a diameter under the resolution limit of optical microscopy (< a few 100 nm). When membrane tension is unaffected, 63.0% of liposomes display tubes only, 2.3% spikes only, while 6.1% of liposomes carry a mix of both, and 28.6% are undetermined (Fig. 1c, non-deflated liposomes). To examine how membrane tension affects the occurrence of tubes and spikes, liposomes are deflated by a hyper-osmotic shock (Methods) before actin polymerization is triggered. This treatment leads to a huge increase in the number of liposomes displaying spikes: 65.0% of deflated liposomes display spikes (with or without tubes), compared to 8.4% in non-deflated conditions (Fig. 1c, $p < 0.0001$). Yet, the frequency with which tubes (with or without spikes) are observed is essentially unaffected: 69.1% for non-deflated liposomes compared to 74.8% for deflated liposomes (not significant, $p = 0.24 > 0.05$, Supplementary Fig. 1b). An increase in membrane tension by a hypo-osmotic treatment (Methods) does not change the occurrence of tubes and spikes significantly (Supplementary Fig. 1c).

Membrane tubes and spikes exclusively rely on the presence of the actin network, as they disappear when the network is destructed[7] (Fig. 1, d and e and Methods). A possible effect of membrane pre-curvature induced by pVCA attachment to the membrane is ruled out (Supplementary Information and Supplementary Fig. 2).

Characterization of tubes

To assess where new actin monomers are incorporated during tube growth, we incorporate differently labeled monomers (green) after 20 minutes (Methods). As previously observed for actin networks growing around polystyrene beads [9, 10], new monomers insert at

the liposome surface (Fig. 2a). Strikingly, new (green) monomers are also observed within the already grown (red) actin network (Fig. 2a), indicating new actin incorporation on the sides of membrane tubes (tubes are evidenced by phase contrast imaging, Fig. 2a, top), This observation is confirmed by the localization, along tubes and at the liposome surface, of S-pVCA (Fig. 2b), the Arp2/3 complex (Fig. 2c), and free barbed ends (Supplementary Fig. 3). Moreover, the presence of the Arp2/3 complex everywhere in the whole volume of the actin network demonstrates its dentritic nature (Fig. 2c).

We find that the average length of the longest tubes increases linearly with network thickness (Fig. 3, a and b). In fact, maximal tube length roughly equals the thickness of the actin network, independently of membrane tension (Fig. 3b, slope 0.89 ± 0.04), albeit deflated liposomes produce a smaller actin cortex. Moreover, we find that tubes grow simultaneously with the actin network (Fig. 3, c and d and Supplementary Fig. 4). Tubes shorter than the network thickness are also present, as evidenced by confocal microscopy (Supplementary Fig. 5a).

The origin of the accumulation in membrane fluorescence detected at the tip of some of the longer tubes is unclear. We observe that S-pVCA forms aggregates on membranes and sticks membranes together, even in the absence of actin (Supplementary Fig. 6). It is possible that small vesicles are attached via S-pVCA to the membrane before polymerization starts and are pushed outward by actin growth. However, the presence of different tube lengths (Supplementary Fig. 5) rules out that tubes could be only formed by pre-existing attached vesicles.

Characterization of spikes

We find that new actin is incorporated at the tips of the spikes as well as at the sides (Fig. 4a), consistent with the localization of S-pVCA (Fig. 4b). Spikes are filled in with the Arp2/3

123 complex and CP (Fig. 4c and Supplementary Fig. S7), characteristic of a branched network.
124 A clump of actin is observable at the base of the spikes (Fig. 4d). The thickness of the clump
125 bears no clear correlation with the length of the spikes (Supplementary Fig. 8a), but slightly
126 correlates with their width (Supplementary Fig. 8b). Spikes initially elongate with time until
127 polymerization slows down, the basal width of spikes, however, remains roughly constant
128 over time (Fig. 4e and Supplementary Fig. 8c).
129
130 **Effect of network meshsize and membrane tension**
131 Lowering the Arp2/3 complex or CP concentrations, could, in principle, result in loosening
132 the network, but fails to form a cohesive thick enough (> 500 nm), network[11]. Using the
133 property of profilin to inhibit branching and therefore loosen the actin network[12], we obtain a
134 visible, thick, network comparable to reference conditions (Supplementary Fig. 9a and
135 Methods). We find that the occurrence of tubes is reduced in these conditions (74.8% of
136 liposomes display tubes when profilin is in excess compared to 91.4% in reference
137 conditions, Supplementary Fig. 9b, $p < 0.0001$). Strikingly, decreasing membrane tension in
138 loosened network conditions significantly increases the presence of tubes and spikes
139 (Supplementary Fig. 9b, $p < 0.0001$).
140
141 **Theoretical models for spikes and tubes**
142 The appearance of large-scale membrane deformations (spikes) driven by a uniformly
143 polymerizing actin network is rationalized using analytical modeling and numerical Finite
144 Element calculations (Methods). The actin network behaves as a viscoelastic material with an
145 elastic behavior at short time and a viscous behavior at long time due to network
146 rearrangement, the cross-over time being on the order of 1-10 s [13, 14, 15]. We focus on the
147 viscous behavior as the growth of the network occurs on timescales of tens of minutes.

We model the growth of the actin network with a uniform actin polymerization velocity v_g normal to the liposome membrane (motivated by Fig. 4a) and solve the hydrodynamic force balance equation at low Reynolds number (the "Stokes equation") (Methods). Actin polymerization on a flat membrane results in a uniform actin flow which does not generate any mechanical stress. Small perturbations of membrane shape modulate the actin velocity field and generate viscous stress on the membrane. For a periodic deformation (Fig. 5a, left), the actin stress varies as the square of the deformation amplitude (Methods) in agreement with actin growth on a curved surface[13, 16]. For a localized (Gaussian) membrane perturbation $u(x) = Ae^{-(x/b)^2}$ with amplitude A and width b (Fig. 5a, right), we calculate the pressure and velocity fields in the actin layer numerically (Fig. 5b). Velocity gradients in the growing actin layer, generated by the deformed surface, induce a normal pushing force at the center of the perturbation, and pulling forces at the periphery of the perturbation (Fig. 5c), that amount to a zero net force when integrated over the deformation area. This contrasts with existing models of filopodia formation, which usually consider bundled actin filaments exerting a net pushing force on the membrane that do not precisely address the force balance within the actin network[6, 17, 18]. Here, we do not *a priori* distinguish the detailed structure of the actin network at the membrane from the one in the protrusion, treating the actin network as a continuum.

A scaling analysis of the Stokes equation, confirmed by our numerical calculation, leads to a normal stress at the center of the perturbation ($x=0$) that scales as $\sigma_{nn} \sim -\eta A^2 b^{-3} v_g$, where η is the viscosity of the actin layer (Supplementary Fig. 10, a and b). An intuitive understanding of this scaling behavior is given in Supplementary Information.

The normal stress σ_{nn} is balanced by the membrane elastic restoring stress[19] $\sigma_{memb} = -\gamma C + \kappa \partial_s^2 C$, where γ is the membrane tension, κ the bending rigidity, C the membrane curvature ($\sim A/b^2$) and ∂_s the curvilinear derivative ($\sim 1/b$). Considering that b is larger than the

characteristic length $\lambda = \sqrt{\kappa/\gamma}$, the stress is dominated by membrane tension. The balance of actin polymerization and membrane stresses defines a threshold amplitude $A^* = \gamma b/(\eta v_g)$. When the amplitude of the perturbation is smaller than this threshold ($A < A^*$) the membrane stress dominates and the perturbation relaxes. Above the threshold ($A > A^*$) the force exerted by the network is dominant and the instability develops. We now evaluate whether such a perturbation could be reached by thermal fluctuations characterized by the Boltzmann constant k_B and the temperature *T*. The average membrane thermal roughness at length scales larger than the actin mesh size ξ, characterized by the average of the gradient of the membrane shape ∇h, is given by $< |\nabla h|^2 > \sim \frac{k_B T}{4\pi\kappa} \log\left(\left(\frac{2\pi\lambda}{\xi}\right)^2 + 1\right)$ [19]. Identifying $< |\nabla h|^2 >$ with $(A/b)^2$ (provided λ and ξ are on the same order), spikes are predicted below a threshold tension: $\gamma^* \approx \eta v_g \sqrt{k_B T/(4\pi\kappa)}$. Evaluating actin network viscosity η as the product of the elastic modulus (*E*) times the viscoelastic relaxation time (τ_{ve}) : $\eta \approx E\tau_{ve} \approx 10^4\ Pa\ s$ (with $E \approx 10^4\ Pa$ [20] and $\tau_{ve} \approx 1\ s$ [14, 15]), $\kappa \approx 10 k_B T$ and $v_g \approx 10^{-9}\ m/s$ (Fig. 3d, note that this velocity is lower than the polymerization of a single actin filament because the network grows under stress[16]), we find $\gamma^* \approx 10^{-6}\ N/m$. This value is in the range of membrane tension for non-deflated liposomes[21], but is larger than the tension of deflated liposomes, leading to the prediction that deflated liposomes are prone to the formation of spikes, in agreement with our experimental results (Fig. 1c). Spike initiation also depends on the structure of the actin network through the value of the network viscosity η. Using the relationship[22]: $\eta \approx k_b T l_p \tau_{ve}/\xi^4$, with $l_p$the persistence length of the actin filament ($\sim 10\ \mu m$)[23], we find the following condition for spike initiation:

$$\gamma \xi^4 < k_B T l_p v_g \tau_{ve} \sqrt{\frac{k_B T}{2\pi\kappa}} \qquad \text{Eq.1}$$

In contrast to "thin" spike-like protrusions[6], the spikes we consider here are formed by the growth of a branched network with a uniform polymerization along the liposome membrane (Fig. 4). The compressive stress resulting from actin polymerization (shown in Fig. 5b) explains that spikes are much wider than the ones previously observed[6], and that they grow faster than the surrounding actin layer (Supplementary Information and Fig. 4).

The initiation of membrane tubes in reference condition requires a pulling force at the tip of the tube larger than $f_{tube} = 2\pi\sqrt{2\kappa\gamma} \sim 2\ pN$ [24, 25] (Fig. 5d with above estimates). The tube radius ($r_{tube} = \sqrt{\kappa/(2\gamma)} \sim 20\ nm$) is smaller than the size of the actin mesh through which it is pulled. This situation differs from spikes where the flow of the actin network is enslaved to the shape of the membrane, thus generating a wider deformation. In our case, tube pulling requires physical attachment of the actin to the membrane through the activator pVCA[26]. The force exerted by the growth of the actin network (moving away from the liposome surface at a velocity v_g) on the filament bound to the tip of the tube (moving at a velocity $\dot{L}$) is equivalent to a friction force (Supplementary Information), which can be crudely estimated using the Stokes law: : $f_{drag} = 6\ \pi\eta r_{tube}(v_g - \dot{L})$ (Fig. 5e). At steady-state, this force has to balance the tube force f_{tube} (Fig. 5f), giving the tube extraction velocity, $\dot{L} = v_g\left(1 - \frac{f_{tube}}{6\ \pi\eta r_{tube} v_g}\right)$. Tube extraction is possible provided $\dot{L} > 0$. This is indeed the case for liposomes under reference conditions ($\gamma \sim 10^{-6}$ N/m), for which $6\ \pi\eta r_{tube} v_g = 6\ \pi\eta(\frac{f_{tube}}{4\pi\gamma})v_g = \frac{3\eta v_g}{2\gamma} f_{tube} \approx 10\ f_{tube}$ (with above estimates). Note that ($\dot{L} \gtrsim 0.9 v_g$) explaining why tubes initiated early during actin growth actually span the entire actin layer. A ten-fold increase of membrane tension could in principle prevent tube formation. Hypo-tonic treatment does not change the occurrence of tubes (Supplementary Fig. 1c), suggesting that the tension does not

reach a sufficiently high level under these conditions. Using the relationship[22]: $\eta \approx k_B T l_p \tau_{ve}/\xi^4$ the condition for tube extraction is :

$$\gamma \xi^4 < \frac{3}{2} k_B T l_p v_g \tau_{ve} \qquad \text{Eq.2}$$

(Supplementary Fig. 10d). Increasing the actin mesh size indeed significantly reduces the occurrence of membrane tubes (Supplementary Fig. 9). Omitting CP, in principle, also decreases network mesh size, and no membrane tubes have been reported in these conditions[6, 27]. In yeast, actin is absolutely required for endocytosis, likely because of the high turgor pressure that opposes inward membrane deformations [28, 29, 30]. The force needed to overcome the turgor pressure can reach 1000 pN [31], almost three orders of magnitude larger than the actin force in our *in-vitro* conditions. Using yeast relevant parameters for actin dynamics (polymerization velocity $v_p = 50nm/s$ [1] and actin network viscosity $\eta = 10^5\ Pa.s$ as estimated from the same scaling law as above and with a Young's modulus $E \approx 10^4\ Pa$, for an actin network in cell extracts[32] and $\tau_{ve} \approx 10\ s$), the drag force generated by the actin network on a tube of radius *r=10nm* is on the *nN* order. It is thus in principle able to overcome the turgor pressure and to trigger membrane deformation leading to endocytosis (Supplementary Information).

The cell is a robust system where redundant mechanisms ensure proper function, which makes detailed cell mechanisms difficult to decipher. This is true for membrane deformations into filopodia [5] or endocytic intermediates [1]. Here, we show that a branched actin network growing at a membrane is able to mimic the initiation of either an endocytosis-like or a dendritic filopodia-like deformation. Our results support recent findings that the initiation of dendritic filopodia and endocytosis primarily relies on the growth of a branched actin network [1, 3, 5].

242 Endocytosis is intimately dependent on the existence of a physical link between the actin
243 network and the plasma membrane in yeast as well as in mammalian cells under high cell
244 tension. Controlled endocytosis is abolished in yeast if this link is suppressed, although
245 already endocytosed vesicles retain their extraordinary capacity to polymerize actin and even
246 undergo actin-based motility [3, 33]. In our reconstituted system, the membrane-pVCA-network
247 linkage is essential to produce tubes, as the absence of one of these links precludes tubular
248 membrane deformation (Supplementary Information, Supplementary Fig. 2a, and Fig. 5d). In
249 fact, the pVCA region interacts with branched actin networks both through the binding of the
250 Arp2/3 complex[26] and through tethering of actin filament free barbed ends[34]. Note that
251 another form of pVCA was shown to induce clustering and phase-separation of lipids in the
252 absence of CP, but not membrane deformations[26]. Here we show that, through our
253 membrane-pVCA-network linkage, actin dynamics alone have the remarkable capacity to
254 initiate endocytosis-like membrane deformations with a width smaller than, or of the order of,
255 the actin mesh size.
256
257 A class of model for filopodia initiation assumes a particular actin organization in the
258 protrusion, typically that of bundled actin filaments [6, 17, 18, 35, 36]. Supported by our dual color
259 actin measurements and by labeling of the Arp2/3 complex and CP, our model for spike
260 initiation assumes that actin polymerization occurs uniformly at the membrane, which
261 indicates that new actin is incorporated all along the conical membrane surface, and not only
262 at the tip of the protrusion as observed in Liu[6]. Moreover, our characterization reveals that
263 the actin network is branched during the entire growth process. Decreasing membrane tension
264 decreases the critical amplitude for spike nucleation and increases the likelihood of spike
265 formation (Fig. 6) oppositely to thin actin filament protrusions[6], thus revealing the very
266 different nature of these two types of protrusions, both in their initiation, and in their

subsequent growth dynamics. Spikes are mimics of filopodia, especially in the case of dendritic filopodia whose formation relies on the Arp2/3 complex-branched network [37].

Our experimental and theoretical results are summarized in Fig. 6, where the threshold for spikes and tube formation (Eq.1 and Eq.2) are shown together with the explored experimental conditions. We conclude that tubes and spikes co-exist at low tension or low mesh size whereas we predict that they do not form at high tension and high mesh size. At intermediate tension and meshsize, only tubes form, but not spikes. We thus highlight how membrane deformations induced by actin polymerization can be modulated by the interplay between membrane tension and actin network mesh size.

Methods

1. Reagents, lipids, proteins

Chemicals are purchased from Sigma Aldrich (St. Louis, MO, USA) unless specified otherwise. L-alpha-phosphatidylcholine (EPC), 1,2-distearoyl-sn-glycero-3-phosphoethanolamine-N-[biotinyl polyethylene glycol 2000] (biotinylated lipids), 1,2-dioleoyl-sn-glycero-3- [[N(5-amino-1-carboxypentyl)iminodiacetic acid]succiny] nickel salt (DOGS-NTA-Ni) are purchased from Avanti polar lipids (Alabaster, USA). Texas Red® 1,2-dipalmitoyl-sn-glycero-3-phosphocholine, triethylammonium salt is from Thermofisher. Actin is purchased from Cytoskeleton (Denver, USA) and used with no further purification. Fluorescent Alexa Fluor 488 actin conjugate and Alexa Fluor 546 actin conjugate are obtained from Molecular Probes (Eugene, Oregon, USA). Porcine Arp2/3 complex is purchased from Cytoskeleton and used with no further purification. Biotin is purchased from Sigma-Aldrich (St. Louis, Missouri, USA), diluted in DMSO. Mouse $\alpha 1\beta 2$ capping protein is purified as in [38]. Untagged human profilin and S-pVCA (where pVCA is the proline rich

292 domain-verprolin homology-central-acidic sequence from human WASP, starting at amino
293 acid Gln150) are purified as in [8] . S-pVCA is fluorescently labeled on the N-terminal amine
294 with Alexa Fluor 546 at pH 6.5 for 2 h at 4°C, desalted and then purified on a Superdex 200
295 column. His-pVCA-GST (GST-pVCA) is purified as for PRD-VCA-WAVE [39] and His-
296 pVCA is essentially the same without the glutathione sepharose step. Mouse α1β2 capping
297 protein is fluorescently labeled with Alexa Fluor 488 C_5-maleimide (ratio of 1:1
298 protein:label) for 1h at room temperature and then at 4°C overnight under agitation. Porcine
299 Arp2/3 complex is fluorescently labeled with Alexa Fluor 488 C_5-maleimide (ratio of 1:10
300 protein:label) at pH 7.2 for 3h on ice and then purified on a PD Minitrap G-25 column.
301 A solution of 30 μM monomeric actin containing 15% of labeled Alexa Fluor 488 actin
302 conjugate is obtained by incubating the actin solution in G-Buffer (2 mM Tris, 0.2 mM
303 $CaCl_2$, 0.2 mM DTT, 0.2 mM ATP, pH 8.0) overnight at 4°C. All proteins (S-pVCA, profilin,
304 CP, actin) are mixed in the isotonic, hypertonic or hypotonic working buffer. The isotonic
305 working buffer contains 25 mM imidazole, 70 mM sucrose, 1 mM Tris, 50 mM KCl, 2 mM
306 $MgCl_2$, 0.1 mM DTT, 1.6 mM ATP, 0.02 mg/mL β-casein, adjusted to pH 7.4. The
307 hypertonic, isotonic, and hypotonic working buffers differ only by their sucrose concentration
308 (hypertonic:320 mM sucrose; isotonic: 70 mM sucrose; hypotonic: no sucrose). Osmolarities
309 of the hypertonic, isotonic, and hypotonic working buffers are respectively 400, 200, and 95
310 mOsmol, as measured with a Vapor Pressure Osmometer (VAPRO 5600). In case of
311 experiments with DOGS-NTA-Ni lipids, all proteins are diluted in a working buffer
312 containing 280 mM glucose, 10 mM HEPES, 0.5 mM DABCO, 100 mM KCl, 4 mM $MgCl_2$,
313 1 mM DTT, 10 mM ATP and 0.05 mg/mL β-casein.
314 **2. Liposome preparation**
315 Liposomes are prepared using the electroformation technique. Briefly, 10 μl of a mixture of
316 EPC lipids, 0.1% biotinylated lipids or 5% DOGS-NTA-Ni lipids, and 0.1% TexasRed lipids

with a concentration of 2.5 mg/ml in chloroform/methanol 5:3 (v/v) are spread onto indium tin oxide (ITO)-coated plates under vacuum for 2 h. A chamber is formed using the ITO plates (their conductive sides facing each other) filled with a sucrose buffer (0.2 M sucrose, 2 mM Tris adjusted at pH 7.4) and sealed with hematocrit paste (Vitrex Medical, Denmark). Liposomes are formed by applying an alternate current voltage (10 Hz, 1 V) for 2 h. Liposomes are then incubated with an activator of actin polymerization (S-pVCA, 350 nM) via a streptavidin-biotin link for 15 min. Isotonic liposomes are used right away for polymerizing actin in the isotonic working buffer. To obtain deflated or tense liposomes, an extra step is added: they are diluted twice in the hypertonic (400 mOsmol) or hypotonic (95 mOsmol) working buffer respectively and incubated for 30 min. The final solution is therefore at 300 mOsmol or 110 mOsmol respectively.

3. Biotin-blocking experiments

S-pVCA labeled with AlexaFluor546 and biotin are diluted in the isotonic working buffer and incubated for 10 min to reach final concentration of 350 nM S-pVCA and various concentrations of biotin (87.5 nM, 175 nM, 262.5 nM, 350 nM). Note that 350 nM of biotin corresponds to a full saturation of the streptavidin sites of S-pVCA. Unlabeled liposomes (99.9% EPC lipids, 0.1% biotinylated lipids) are then diluted twice in this solution and incubated for 15 min. Tubes and spikes are visualized by the fluorescence of S-pVCA.

4. Actin cortices with a branched network

Our condition of reference ("reference condition") corresponds to condition 1 and non-deflated liposomes.

Condition 1: Actin polymerization is triggered by diluting the non-deflated, deflated or tense liposomes 6 times in a mix of respectively isotonic, hypertonic, or hypotonic working buffer containing final concentrations of 3 μM monomeric actin (15% fluorescently labeled with Alexa Fluor 488), 3 μM profilin, 37 nM Arp2/3 complex, 25 nM CP. Note that the final

concentrations of salt and ATP in all conditions (isotonic, hypertonic, hypotonic) are 0.3 mM NaCl, 41 mM KCl, 1.6 mM $MgCl_2$, 0.02 mM $CaCl_2$ and 1.5 mM ATP.

Condition 2: Same protocol as in Condition 1 with unlabeled monomeric actin, unlabeled liposomes (99.9% EPC lipids, 0.1% biotinylated lipids) and S-pVCA labeled with Alexa Fluor 546.

In Figure 1, panel c, non-deflated liposomes n=311 are distributed as follows: 215 from 3 experiments in Condition 1 and 96 from 2 experiments in Condition 2. Deflated liposomes n=123 are distributed as follows: 92 from 2 experiments in Condition 1 and 31 from one experiment in Condition 2.

Condition 3: Same protocol as in Condition 1 with unlabeled monomeric actin and Arp2/3 complex labeled with Alexa Fluor 488 C_5-maleimide.

Condition 4: Same protocol as in Condition 1 with unlabeled monomeric actin and capping proteins labeled with Alexa Fluor 488 C_5-maleimide.

5. Actin cortices with a loosened branched network

Actin polymerization is triggered the same way as above (condition 1), except with 15 μM profilin (instead of 3), and during a longer time (overnight instead of 1-2 hours). Reference conditions correspond to non-deflated liposomes in condition 1, except that observation is done 20 hours after the initiation of polymerization.

6. Photo-damage of the actin network

The actin network area to photo-damage is defined with a diaphragm. The area is illuminated for 15 s with a Hg lamp and a FITC filter cube and the illumination is repeated until actin is completely destroyed or at least no longer detectable by eye.

7. Two color experiment

Liposomes are first incubated with 350 nM S-pVCA for 15 min. This solution is then diluted 3-fold into a mix of isotonic buffer containing 3 μM actin (15% Alexa568-labeled, red), 37

nM Arp2/3 complex and 25 nM CP. After 20 min of incubation in these conditions, the solution is diluted 3 times in a mix of same protein concentrations containing 15% Alexa488-labeled actin, green.

8. Free actin filament barbed end labeling

S-pVCA-activated liposomes (labeled membrane) are placed in a mix containing 3 μM unlabeled monomeric actin, 37 nM unlabeled Arp2/3 complex and 25 nM unlabeled CP. After 20 min of incubation in these conditions, the solution is diluted 5 times in the working buffer to stop actin polymerization. This solution is then incubated with 75 nM labeled capping proteins. Image acquisition is done right after the addition of fluorescently labeled capping proteins.

9. Cryo-electron microscopy

To prepare small liposomes, a mixture of EPC lipids and 0.1% biotinylated lipids with a concentration of 1 mg/mL in chloroform/methanol 5:3 (v/v) is dried and resuspended under vortexing in a buffer containing 25 mM imidazole, 1 mM Tris, 50 mM KCl, 2 mM $MgCl_2$, 0.1 mM DTT, 1.6 mM ATP, 0.02 mg/mL β-casein. Liposomes are then incubated with S-pVCA (350 nM) for 15 min and finally flash-frozen for cryo-electron microscopy. Images were recorded under low dose conditions with a Tecnai G2 Lab6 electron microscope operating at 200 kV with a TVIPS F416 4K camera and with a resolution of 0.21 Å/pixel.

10. Observation of liposomes

Observation in 2D: epifluorescence (GFP filter cube, excitation 470 nm, emission 525 nm; Texas red filter cube: excitation 545-580 nm, emission 610 nm-IR), phase contrast and bright-field microscopy are performed using an IX70 Olympus inverted microscope with a 100x or a 60x oil-immersion objective. Images are collected by a charge coupled device CCD camera (CoolSnap, Photometrics, Roper Scientific).

Observation in 3D: confocal and bright-field microscopy are performed using an inverted Confocal Spinning Disk Roper/Nikon with a 100x or a 60x oil-immersion objective and lasers with wavelengths of 491 nm for actin and 561 nm for lipids. A FITC filter cube (excitation filter: 478-495 nm/emission filter: 510-555 nm) and a TxRed filter cube (excitation filter: 560-580 nm/emission filter: 600-650 nm) are used to acquire respectively actin and lipids fluorescence. Images are collected by a charge coupled device CCD camera (CoolSnap HQ2, Photometrics, Roper Scientific).

3D data: Z-stacks are acquired using the software Metamorph on each wavelength with a z-interval of 0.5 μm.

11. Image analyses of liposomes, tubes and spikes

Image analyses are performed with ImageJ software and data are processed on Matlab. The thickness of the actin network and the length of tube membranes is obtained from fluorescence intensity profiles (Fig. 3a). The first peak of the membrane profile determines the liposome surface and the second peak determines the end of the membrane tube. The actin network thickness is the distance between the first peak and the half width at half maximum of the actin fluorescence profile. The length of the membrane tubes is obtained as the peak-to peak distance of the membrane fluorescence profile. The size of spikes (length, width) and actin network is determined by the corresponding positions of the inflexion points. Fluorescence profiles in each case (membrane, actin) are fitted with a polynomial function. The first maximum and the second minimum of the fit derivative, corresponding to inflexion points of the profile, determine the membrane or actin edges. The size is then the distance between the two edges. From actin fluorescence profile, actin network thickness at the base of spike is defined as the distance between the first maximum and first minimum of the fit derivative.

To determine whether shorter tubes are present in addition to the easily visualized long ones, we measure the total fluorescence intensity of the membrane on an arc that is displaced along a radial axis r from close to the liposome surface to the external part of the network. We hypothesize that tubes maintain a constant diameter along their length, as is established for pure membrane tubes [24]. In these conditions, if all tubes have the same length, the total intensity should show a plateau as a function of r, until falling off to zero at an r where there are no more tubes (Supplementary Fig. 4a). Conversely, the total intensity would decrease as a function of r if tubes of different lengths were present (Supplementary Fig. 4a).

12. Statistical analyses

All statistical analyses are performed using MedCalc software. N-1 Chi-squared test is used to determine the statistical significance. Differences among samples were considered statistically significant when $p < 0.05$.

13. Theoretical model for spike initiation

To calculate the stress exerted by a viscous network, polymerizing at a curved surface we consider an incompressible Stokes flow, described by force balance and incompressibility, i.e., $\vec{\nabla} \cdot \vec{\sigma} = 0$ and $\vec{\nabla} \cdot \vec{v} = 0$, where $\vec{v}$ is the velocity of the network and $\vec{\sigma}$ is the viscous stress in Cartesian coordinates, given by, $\sigma_{ij} = -p\,\delta_{ij} + \eta\left(\frac{\partial v_i}{\partial x_j} + \frac{\partial v_j}{\partial x_i}\right)$. Polymerization of the actin network is encoded in this model by imposing the velocity of the network, normal to the surface of the curved interface. Moreover, we impose a stress free boundary condition at the outer layer, both for the normal as well as the tangential stress, i.e., $\sigma_{nn} = 0$ and $\sigma_{nt} = 0$. Note that, in the limit we consider, an infinite thick network, this corresponds to a uniform velocity in the z-direction.

We determine the first order correction of the normal stress on a deformed surface characterized by $u(x) = u_0 \exp(iqx)$ along the x axis (u_0 is the deformation amplitude and q the wave vector, Fig. 5a, left). We seek a solution for the velocity field within the network of

440 the form $v_j = v_j(z)\exp(iqx)$, where the index *j* represents the coordinate *x* or z, and a
441 pressure field of the form $p = p(z)\exp(iqx)$. Assuming that the network grows normal to
442 the surface, the first order correction of the *x*-component of the velocity field satisfies the
443 boundary condition $\delta v_x(z = 0) = -v_g \partial_x u(x)$ at the interface (*z=0*). We assume here a
444 network of large thickness and require that the first order correction to the velocity vanishes
445 at $z \to \infty$. The first order corrections to the velocity and pressure in the network
446 read $\delta v_x(z) = -iqu_0(1 - qz)v_g\exp(-qz)$,$\delta v_z(z) = -q^2 u_0 v_g z\exp(-qz)$ and $\delta p(z) =$
447 $-2\,\eta\, q^2 u_0 v_g \exp(-qz)$. At this order the actin normal stress turns out to vanish at any point
448 of the liposome surface: $\sigma_{nn}(x, z = 0) = 2\eta\partial_z v_z - p = 0$. This implies that the membrane is
449 linearly stable against small deformations in the presence of a growing actin network.
450 The second-order correction for the actin stress is in principle difficult to calculate, as the
451 different modes of deformation are coupled. An analytical estimate can be obtained by
452 expanding the surface normal vector up to second order, which yields the following scaling
453 for the normal stress at the liposome surface, $\sigma_{nn} \propto -\eta q^3 u_0^2 v_g$. This weakly non-linear
454 analysis reveals that there is a non-zero normal stress acting on the membrane, which we will
455 later compare with the membrane contribution to address system stability.
456 In order to get a numerical solution for the normal stress in a "localized" spike-like
457 perturbation on the interface, as opposed to the periodic one presented above, we use a Finite
458 Element Method from *Mathematica* with default settings. We implement a geometry as
459 described in Fig. 5a (right), where the lower surface is parametrized with a Gaussian
460 deformation as mentioned before, i.e, $u(x, z) = z - A\exp-\left(\frac{x}{b}\right)^2 = 0$ and we choose the
461 height of the system to be much larger that the extend and amplitude of the perturbation
462 ($h = 2\mu m$). Note that here, b, the characteristic lateral length of the localized perturbation, is
463 related to the wavenumber $q \sim 1/b$ used for the linear analysis. To account for a constant

polymerization, perpendicular to the lower surface we impose the velocity on the lower surface, i.e., $\partial v(u(x,z)=0) = v_g(\partial_x u(x,z)\hat{x} + \partial_z u(x,z)\hat{z})$, where v_g is the normalized polymerization velocity and a vanishing normal and tangential stress at the upper boundary $z = h$, i.e., $\sigma_{nn}(z=h) = 0$ and $\sigma_{nt}(z=h) = 0$. Using this approach we could find the same scaling with amplitude and width of the perturbation, as found for the weakly non-linear analysis for a sinusoidal perturbation. Note also that here, by imposing the normal velocity at the interface, a choice that is motivated by the dual color images in Fig. 4a, we do not impose the tangential stress on the membrane, and hence this stress has to be balanced by an in-plane viscous stress in the membrane, which at this stage we do not model. These FEM simulations allow us to visualize the velocity field as well as the pressure throughout the network, indicating the increase in pressure inside the local perturbation caused by the local convergence of the velocity fields (Fig. 5b).

Data availability

The data that support the plots within this paper and other findings of this study are available from the corresponding author upon request.

References

1. Kukulski W, Schorb M, Kaksonen M, Briggs JA. Plasma membrane reshaping during endocytosis is revealed by time-resolved electron tomography. *Cell*, **150**(3)**:** 508-520 (2012).

2. Picco A, Mund M, Ries J, Nedelec F, Kaksonen M. Visualizing the functional architecture of the endocytic machinery. *Elife*, **4:** (2015).

3. Picco A, Kukulski W, Manenschijn HE, Specht T, Briggs JAG, Kaksonen M. The contributions of the actin machinery to endocytic membrane bending and vesicle formation. *Molecular Biology of the Cell*, **29**(11)**:** 1346-1358 (2018).

4. Boulant S, Kural C, Zeeh JC, Ubelmann F, Kirchhausen T. Actin dynamics counteract membrane tension during clathrin-mediated endocytosis. *Nat Cell Biol*, **13**(9)**:** 1124-1131 (2011).

5. Korobova F, Svitkina T. Molecular architecture of synaptic actin cytoskeleton in hippocampal neurons reveals a mechanism of dendritic spine morphogenesis. *Mol Biol Cell*, **21**(1)**:** 165-176 (2010).

6. Liu AP, Richmond DL, Maibaum L, Pronk S, Geissler PL, Fletcher DA. Membrane induced bundling of actin filaments. *Nature Physics*, **4:** 789-793 (2008).

7. van der Gucht J, Paluch E, Plastino J, Sykes C. Stress release drives symmetry breaking for actin-based movement. *Proc Natl Acad Sci U S A*, **102**(22)**:** 7847-7852 (2005).

8. Carvalho K, Lemiere J, Faqir F, Manzi J, Blanchoin L, Plastino J*, et al.* Actin polymerization or myosin contraction: two ways to build up cortical tension for symmetry breaking. *Philos Trans R Soc Lond B Biol Sci*, **368**(1629)**:** 20130005 (2013).

9. Paluch E, Piel M, Prost J, Bornens M, Sykes C. Cortical actomyosin breakage triggers shape oscillations in cells and cell fragments. *Biophys J*, **89**(1)**:** 724-733 (2005).

10. Akin O, Mullins RD. Capping protein increases the rate of actin-based motility by promoting filament nucleation by the Arp2/3 complex. *Cell*, **133**(5)**:** 841-851 (2008).

11. Kawska A, Carvalho K, Manzi J, Boujemaa-Paterski R, Blanchoin L, Martiel JL*, et al.* How actin network dynamics control the onset of actin-based motility. *Proc Natl Acad Sci U S A*, **109**(36)**:** 14440-14445 (2012).

12. J P, S S, A J, B G, MF C. - Profilin Interaction with Actin Filament Barbed End Controls Dynamic Instability. *Dev Cell*, **36**(2)**:** 201-214 (2016).

13. Julicher F, Kruse K, Prost J, Joanny JF. Active behavior of the cytoskeleton. *Physics reports*, **449**(1-3)**:** 3-28 (2007).

14. Gardel ML, Shin JH, MacKintosh FC, Mahadevan L, Matsudaira PA, Weitz DA. Scaling of F-actin network rheology to probe single filament elasticity and dynamics. *Phys Rev Lett*, **93**(18)**:** 188102 (2004).

15. Gardel ML, Kasza KE, Brangwynne CP, Liu J, Weitz DA. Chapter 19: Mechanical response of cytoskeletal networks. *Methods Cell Biol*, **89:** 487-519 (2008).

16. Noireaux V, Golsteyn RM, Friederich E, Prost J, Antony C, Louvard D*, et al.* Growing an actin gel on spherical surfaces. *Biophys J*, **78:** 1643-1654 (2000).

17. Mogilner A, Rubinstein B. The physics of filopodial protrusion. *Biophys J*, **89**(2)**:** 782-795 (2005).

18. Prost J, Barbetta C, Joanny JF. Dynamical control of the shape and size of stereocilia and microvilli. *Biophys J*, **93**(4)**:** 1124-1133 (2007).

19. Deserno M. Fluid lipid membranes: from differential geometry to curvature stresses. *Chem Phys Lipids*, **185:** 11-45 (2015).

20. Marcy Y, Prost J, Carlier M-F, Sykes C. Forces generated during actin-based propulsion: a direct measurement by micromanipulation. *Proc Natl Acad Sci USA*, **101**(16)**:** 5993-5997 (2004).

21. Caorsi V, Lemiere J, Campillo C, Bussonnier M, Manzi J, Betz T*, et al.* Cell-sized liposome doublets reveal active tension build-up driven by acto-myosin dynamics. *Soft Matter*, **12**(29)**:** 6223-6231 (2016).

22. Kroy K, Frey E. Force-Extension Relation and Plateau Modulus for Wormlike Chains. *Phys Rev Lett*, **77**(2)**:** 306-309 (1996).

23. Isambert H, Venier P, Maggs AC, Fattoum A, Kassab R, Pantaloni D*, et al.* Flexibility of actin filaments derived from thermal fluctuations. *J Biol Chem*, **270:** 11437-11444 (1995).

24. Derenyi I, Julicher F, Prost J. Formation and interaction of membrane tubes. *Phys Rev Lett*, **88**(23)**:** 238101 (2002).

25. Roux A, Cuvelier D, Nassoy P, Prost J, Bassereau P, Goud B. Role of curvature and phase transition in lipid sorting and fission of membrane tubules. *Embo J*, **24**(8)**:** 1537-1545 (2005).

26. Smith BA, Padrick SB, Doolittle LK, Daugherty-Clarke K, Correa IR, Jr., Xu MQ*, et al.* Three-color single molecule imaging shows WASP detachment from Arp2/3 complex triggers actin filament branch formation. *Elife*, **2:** e01008 (2013).

27. Liu AP, Fletcher DA. Actin polymerization serves as a membrane domain switch in model lipid bilayers. *Biophys J*, **91**(11)**:** 4064-4070 (2006).

28. Wang X, Carlsson AE. A master equation approach to actin polymerization applied to endocytosis in yeast. *PLoS Comput Biol*, **13**(12)**:** e1005901 (2017).

29. Carlsson AE. Membrane bending by actin polymerization. *Curr Opin Cell Biol*, **50:** 1-7 (2017).

30. Aghamohammadzadeh S, Ayscough KR. Differential requirements for actin during yeast and mammalian endocytosis. *Nat Cell Biol*, **11**(8)**:** 1039-1042 (2009).

31. Dmitrieff S, Nedelec F. Membrane Mechanics of Endocytosis in Cells with Turgor. *PLoS Comput Biol*, **11**(10)**:** e1004538 (2015).

32. Gerbal F, Chaikin P, Rabin Y, Prost J. An Elastic Analysis of *Listeria monocytogenes* Propulsion. *Biophys J*, **79:** 2259 (2000).

33. Sun Y, Leong NT, Jiang T, Tangara A, Darzacq X, Drubin DG. Switch-like Arp2/3 activation upon WASP and WIP recruitment to an apparent threshold level by multivalent linker proteins in vivo. *Elife*, **6:** (2017).

34. Co C, Wong D, Gierke S, Chang V, Taunton J. - Mechanism of actin network attachment to moving membranes: barbed end capture by. *Cell*, **128**(5)**:** 901-913 (2007).

35. Lan Y, Papoian GA. The stochastic dynamics of filopodial growth. *Biophys J*, **94**(10)**:** 3839-3852 (2008).

36. Atilgan E, Wirtz D, Sun SX. Mechanics and dynamics of actin-driven thin membrane protrusions. *Biophys J*, **90**(1)**:** 65-76 (2006).

37. Hotulainen P, Llano O, Smirnov S, Tanhuanpää K, Faix J, Rivera C*, et al.* Defining mechanisms of actin polymerization and depolymerization during dendritic spine morphogenesis. *The Journal of Cell Biology*, **185**(2)**:** 323 (2009).

38. Palmgren S, Ojala PJ, Wear MA, Cooper JA, Lappalainen P. Interactions with PIP2, ADP-actin monomers, and capping protein regulate the activity and localization of yeast twinfilin. *J Cell Biol*, **155**(2)**:** 251-260 (2001).

39. Havrylenko S, Noguera P, Abou-Ghali M, Manzi J, Faqir F, Lamora A*, et al.* WAVE binds Ena/VASP for enhanced Arp2/3 complex–based actin assembly. *Molecular Biology of the Cell*, **26**(1)**:** 55-65 (2015).

Acknowledgments

We acknowledge Dr. Agnieszka Kawska at IlluScientia.com for the Fig.s. We thank Julien Pernier for suggesting the excess profiling experiment for loosening the actin network. This work was supported by the French Agence Nationale pour la Recherche (ANR), grant ANR 09BLAN0283 and ANR 12BSV5001401, by Fondation pour la Recherche Médicale (FRM), grant DEQ20120323737, by the LabEx CelTisPhyBio postdoctoral fellowship (ML), No. ANR-10-LBX-0038 part of the IDEX PSL NANR- 10-IDEX-0001-02 PSL, by Marie Curie Integration Grant PCIG12-GA-2012-334053, “Investissements d'Avenir” LabEx PALM (ANR-10-LABX-0039-PALM), ANR grant ANR-15-CE13-0004-03 and ERC Starting Grant 677532. Our groups belong to the CNRS consortium CellTiss. This work was supported by grants from the French National Research Agency through the “Investments for the Future” (France-BioImaging, ANR-10-INSB-04), the PICT-IBiSA Institut Curie (Paris, France)

Author contributions: CS, RK and VC have equal contributions. CS, VC performed experiments, analyzed data. RK performed the development of theoretical models. AA and MAG, JM, AdC, DL, CC, JP contributed to experimental data, ML and JFJ contributed to the development of the model, PS and CS designed the research. All authors contributed to write the paper.

Author information: request for material should be addressed to PS and CS (pierre.sens@curie.fr and cecile.sykes@curie.fr)

Figures

Figure 1: Experimental system and observations

a, Scheme of the experimental system; proteins not to scale. **b**, Membrane deformations in both non-deflated (three first rows) and deflated conditions (last row). **c**, Top: liposome deflation. Bottom: number of liposomes displaying different indicated behaviors. Non-deflated liposomes, n=311. Deflated liposomes, n=123. (**d**, **e**) Actin network photo-damage (yellow dashed rectangle) on a liposome displaying membrane tubes (**d**) or spikes (**e**). Phase contrast and epifluorescence microscopy of membrane (TexasRed-DHPE, red) and actin network (Actin-Alexa Fluor 488, green). Scale bars, 5µm.

Figure 2: Actin incorporation during tube formation

a, Left: a red actin network is grown for 20 minutes, then an excess of green actin is added, so green regions indicate newly polymerized actin. Right: corresponding polar plots. **b**,Activator of actin polymerization, S-pVCA. False color image and zoom in (white rectangle); the membrane is indicated with a dashed line. (**a**, **b**) Phase contrast and epifluorescence microscopy of the actin network labeled with actin-Alexa Fluor 568 (red) and actin-Alexa Fluor 488 (green) in (**a**), and of S-pVCA-Alexa Fluor 546 in (**b**). **c**, Confocal images of labeled membrane (TexasRed-DHPE, red) and the Arp2/3 complex (Alexa Fluor 488 C_5-maleimide, green) and zoom in (white rectangle). All scale bars, 5µm.

Figure 3: Tube length compared to network thickness

a, Tube length and actin network thickness are measured from fluorescence intensity profiles (yellow dashed box) of the membrane (TexasRed-DHPE, red) and the actin (Alexa Fluor 488, green) channels (Materials and Methods). **b**, Tube length as a function of actin network thickness. White circles: non-deflated liposomes. Grey circles: deflated liposomes. **c**,

667 Dynamics of tube growth (times indicate elapsed time from the start of actin polymerization).
668 **d**, Fluorescence profile of the thick yellow lines shown in (**c**). Membrane and actin
669 fluorescence intensities plotted over time (indicated). Other examples are shown in
670 Supplementary Fig. 4. (**a**, **d**) Epifluorescence microscopy of membrane (TexasRed-DHPE,
671 red) and actin (Alexa Fluor 488, green). All scale bars, 5μm.
672
673 **Figure 4: Actin incorporation in spikes**
674 **a**, Left: Two color experiment: green regions indicate newly polymerized actin. White
675 squares, zooms. Right: fluorescence intensity profiles of spike length (top, thin yellow dashed
676 box on zoomed image) and width (bottom, thick yellow dashed box on zoomed image). **b**,
677 Activator of actin polymerization, S-pVCA. False color and zoom in (white rectangle). (**a**, **b**)
678 Phase contrast and epifluorescence microscopy of the actin network labeled with actin-Alexa
679 Fluor 568 (red) and actin-Alexa Fluor 488 (green) in (**a**), and of S-pVCA-Alexa Fluor 546 in
680 (**b**). **c**, Confocal images of labeled membrane (TexasRed-DHPE, red) and the Arp2/3
681 complex (Alexa Fluor 488 C_5-maleimide, green) and zoom in (white rectangle). **d**,
682 Epifluorescence images of membrane (TexasRed-DHPE, red) and actin (Alexa Fluor 488,
683 green) during spike growth, as a function of time (time indicated after actin polymerization
684 starts). **e**, Spike length and width over time, spike shown in **d**. Other examples in
685 Supplementary Fig. 8. Dashed lines are guides to the eyes. All scale bars, 5 μm.
686
687 **Figure 5: Model for spike initiation and tube formation**
688 **a**, Scheme of the initiation of a periodic and localized membrane deformation by the growth
689 of the actin network. **b**, Velocity field of a viscous network polymerizing over a membrane
690 with a localized (gaussian) perturbation (amplitude $A=0.1\ \mu m$, width $b=0.2\ \mu m$,
691 polymerization velocity $v_g=1\ nm/s$, viscosity $\eta = 10^4\ Pa.s$). Color, pressure in the network
692 layer. **c**, Corresponding distribution of actin and membrane normal stresses (σ_{nn} and σ_{memb}

693 respectively). **d**, Scheme of a membrane tube pulled by the actin network; blue arrows
694 indicate forces within the actin network. **e**, Velocity field of the actin network pulling the
695 membrane tube. We assume a uniform polymerization v_p at the liposome surface and model
696 the presence of the tube as a disc with radius $r_{tube} = 20\ nm$ at a distance from the membrane
697 $h = 100\ nm$. **f**, Force exerted per filament as a function of the distance to the center of the
698 tube, $\bar{r}$, where we have chosen distance between filaments polymerizing on the surface ξ =
699 *30nm*, f_{tube} *= 2pN,* γ *= 10*$^{-6}$ *N/m* and $\nu = 0.4$.
700
701 **Figure 6: Dependence of membrane deformations on membrane tension and actin**
702 **network mesh size.**
703 Representative images of membrane (TexasRed-DHPE) and actin (Alexa Fluor 488) and
704 schematic diagram of membrane deformations as a function of mesh size ξ and membrane
705 tension γ, derived from the theoretical model (Eqs.1 and 2). R corresponds to reference
706 conditions (dense network, non-deflated liposomes, red dot in diagram); a, b, c and d
707 correspond to other experimental conditions with a different mesh size and membrane tension
708 indicated qualitatively in the diagram. Arrows show in which direction membrane tension or
709 mesh size are changed compared to the reference situation (R). Plain arrows indicate a
710 change in membrane tension without affecting the polymerization conditions. Dashed arrows
711 indicate that the conditions of actin polymerization are changed compared to the reference
712 condition. Scale bars, 5 μm.

Figure 1

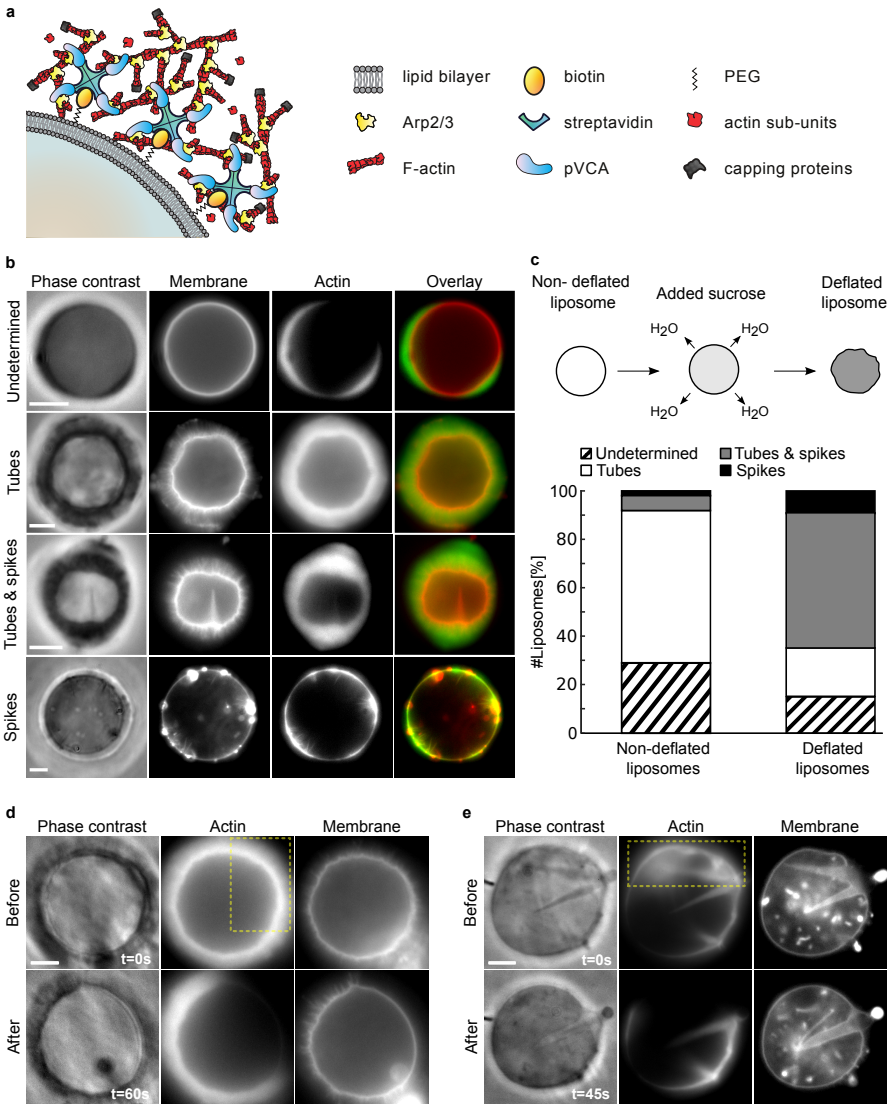
a
lipid bilayer
biotin
PEG
Arp2/3
streptavidin
actin sub-units
F-actin
pVCA
capping proteins
b
Phase contrast
Membrane
Actin
Overlay
Undetermined
Tubes
Tubes & spikes
Spikes
c
Non- deflated liposome
Added sucrose
Deflated liposome
H2O
Undetermined
Tubes
Tubes & spikes
Spikes
#Liposomes[%]
100
80
60
40
20
0
Non-deflated liposomes
Deflated liposomes
d
Phase contrast
Actin
Membrane
Before
After
t=0s
t=60s
e
Phase contrast
Actin
Membrane
Before
After
t=0s
t=45s

Figure 2

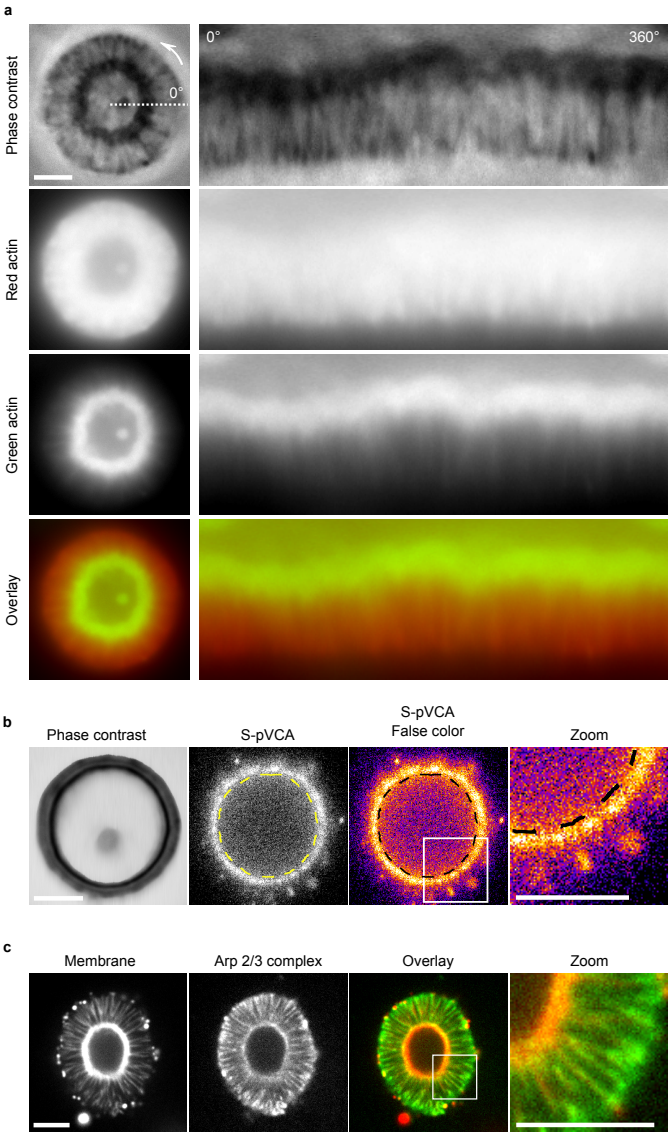
a
Phase contrast
Red actin
Green actin
Overlay
0°
0°
360°
b
Phase contrast
S-pVCA
S-pVCA
False color
Zoom
c
Membrane
Arp 2/3 complex
Overlay
Zoom

Figure 3

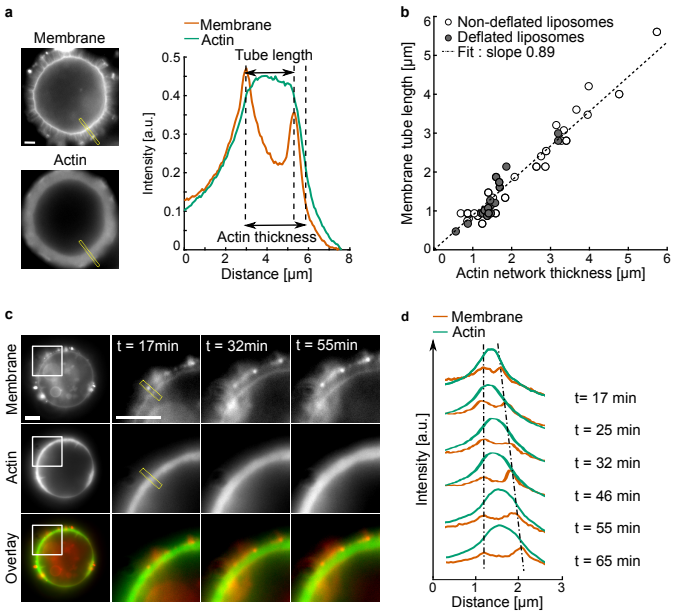
a
Membrane
Actin
Membrane
Actin
Tube length
Actin thickness
Intensity [a.u.]
Distance [µm]
b
Non-deflated liposomes
Deflated liposomes
Fit : slope 0.89
Membrane tube length [µm]
Actin network thickness [µm]
c
Membrane
Actin
Overlay
t = 17min
t = 32min
t = 55min
d
Membrane
Actin
Intensity [a.u.]
Distance [µm]
t= 17 min
t = 25 min
t = 32 min
t = 46 min
t = 55 min
t = 65 min

Figure 4

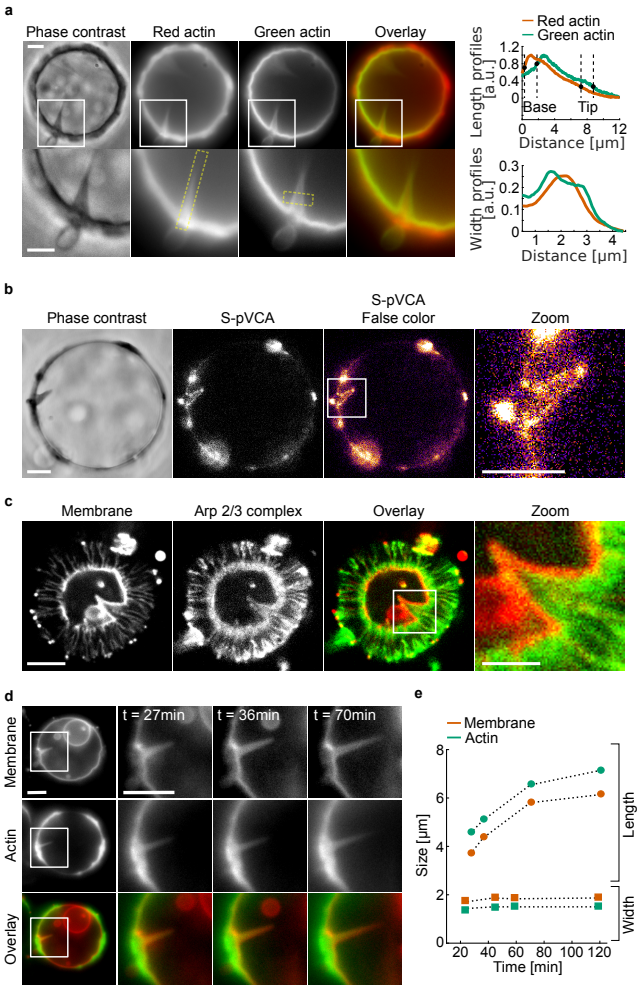
a
Phase contrast
Red actin
Green actin
Overlay
Red actin
Green actin
Length profiles [a.u.]
Base
Tip
Distance [µm]
Width profiles [a.u.]
Distance [µm]
b
Phase contrast
S-pVCA
S-pVCA False color
Zoom
c
Membrane
Arp 2/3 complex
Overlay
Zoom
d
Membrane
Actin
Overlay
t = 27min
t = 36min
t = 70min
e
Membrane
Actin
Size [µm]
Length
Width
Time [min]

Figure 5

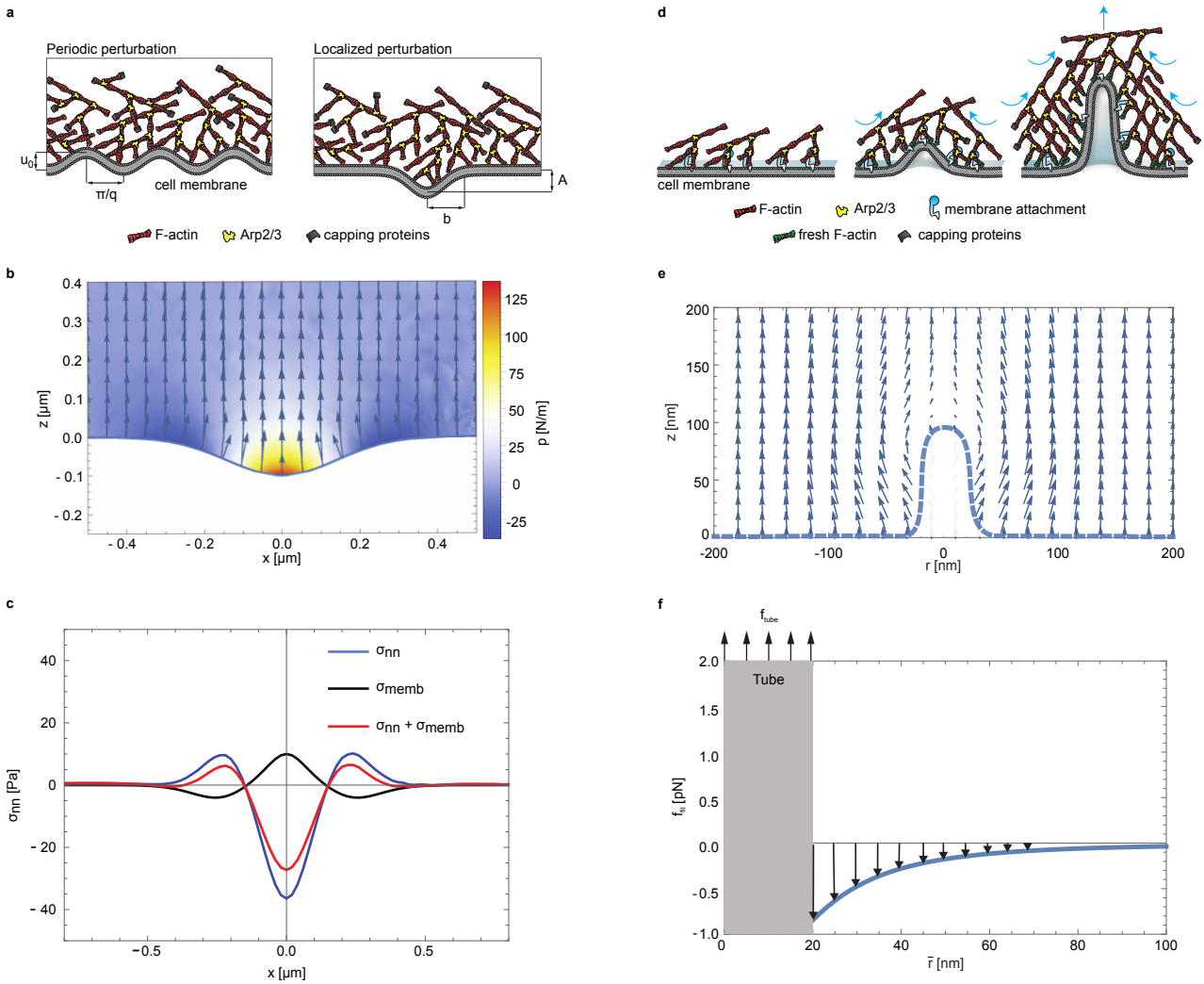
a
Periodic perturbation
Localized perturbation
u0
π/q
cell membrane
A
b
F-actin
Arp2/3
capping proteins
b
z [µm]
x [µm]
p [N/m]
c
σnn
σmemb
σnn + σmemb
σnn [Pa]
x [µm]
d
cell membrane
F-actin
Arp2/3
membrane attachment
fresh F-actin
capping proteins
e
z [nm]
r [nm]
f
ftube
Tube
fti [pN]
r̄ [nm]

Figure 6

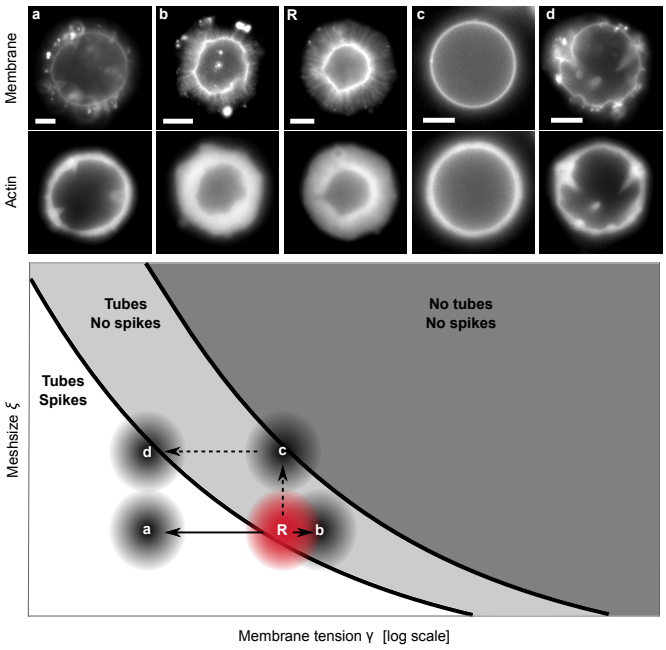
a
b
R
c
d
Membrane
Actin
Tubes
No spikes
No tubes
No spikes
Tubes
Spikes
Meshsize ξ
d
c
a
R
b
Membrane tension γ [log scale]

Supplementary Information

Article: Actin dynamics drive cell-like membrane deformation.

Camille Simon[†1,2], Rémy Kusters[†1,2], Valentina Caorsi[†1,2], Antoine Allard[1,2,3], Majdouline Abou-Ghali[1,2], John Manzi[1,2], Aurélie Di Cicco[1,2], Daniel Lévy[1,2], Martin Lenz[4], Jean-François Joanny[1,2,5], Clément Campillo[3], Julie Plastino[1,2], Pierre Sens[1,2&], Cécile Sykes[1,2&]

[†]These authors contributed equally to this work.
[&]These authors contributed equally to this work.

[1] Laboratoire Physico Chimie Curie, Institut Curie, PSL Research University, CNRS UMR168, 75005, Paris, France. [2] Sorbonne Universités, UPMC Univ Paris 06, 75005, Paris, France. [3] LAMBE, Université Evry, CNRS, CEA, Université Paris-Saclay, Evry F-91025, France. [4] LPTMS, CNRS, Univ. Paris-Sud, Université Paris-Saclay, 91405 Orsay, France.
[5] ESPCI-Paris, 10 rue Vauquelin, 75005, Paris, France.

Possible effect of membrane curvature induced by pVCA attachment

The growth of tubes and spikes seems to be produced exclusively by actin dynamics, independent of curvature proteins. Nevertheless, actin-independent mechanisms may still be at work in our system to induce tube or spike initiation. Indeed, membrane curvature may be induced by the interaction of S-pVCA with the membrane as a tetramer (Fig. 1a), as it is able to bind to 4 biotinylated lipids in the membrane. However, an estimate of the available biotin sites in our experiments reveals that S-pVCA is in excess by about five fold (see next paragraph). Therefore, it is likely that S-pVCA attaches by only one or two links to the membrane. Furthermore, adding biotin in solution to partially saturate S-pVCA does not reduce the production of spikes or tubes although higher amounts of biotin prevent actin polymerization, as expected since the membrane is no longer activated by S-pVCA attachment (Supplementary Fig. 2, a and b). To further rule out the possibility that the S-pVCA-lipid link is somehow producing membrane curvature on its own, we replace the PEGylated-biotinylated lipids normally used to bind the S-pVCA tetramer to the membrane with nickel lipids, to which S-pVCA binds through its histidine tag. This change of protocol does not affect the production of tubes and spikes (Supplementary Fig. 2c, first row). Along similar lines, replacing S-pVCA with other pVCA constructs, the dimer GST-pVCA and the monomeric His-pVCA, both attached to the liposome via nickel lipids, also give rise to the production of tubes and spikes (Supplementary Fig. 2c).
Altogether, these results reveal that changing the oligomerization state of S-pVCA, or the link between S-pVCA and the membrane does not affect the initiation of tubes and spikes. We conclude that the initiation of tubes and spikes does not rely on the deformation of the membrane by S-pVCA alone. Tubes and spikes are therefore a robust feature of actin polymerization through the activation of an actin branched network at a membrane.

Estimates of biotin versus S-pVCA tetramers in the solution of liposomes

Number of biotin per volume unit in the solution containing liposomes (note that they are put in contact with 350 nM of S-pVCA i.e. 87.5 nM tetramers)
Lower estimate:
We first estimate the surface of liposomes S_v per unit volume. The volume of one field of view is 90x70x300 μm^3, the number of liposomes per field of view is 10, the average radius R of a liposome is 7 μm. Therefore, the surface of liposome per volume unit is:

$$S_v = \frac{10 * 4\pi R^2}{90 * 70 * 300 * 10^{-18}} = \frac{10 * 4\pi * 7^2}{90 * 70 * 300 * 10^{-6}} = \frac{10 * 4\pi * 7}{9 * 3 * 10^{-2}} \approx 3 * 10^3 m^{-1}$$

We then estimate the number of biotinylated lipid n_s per unit surface of membrane (liposome). The area of lipid head is 0.4 nm^2 ; the molar percentage of biotinylated lipids is 0.1 % (1/1000), therefore:

$$n_s = \frac{10^{-3}}{4 * 10^{-19}} = 2.5 * 10^{15} m^{-2}$$

The number of biotin per volume unit of solution n_v reads:

$$n_v = n_s * S_v = 2.5 * 10^{15} * 3 * 10^3 \, m^{-3} = 7.5 * 10^{18} \, m^{-3}$$

Concentration of biotin in solution C_{biotin}

Number of Avogadro: $N_a = 6 * 10^{23} \, mol^{-1}$

The concentration of biotin in solution is therefore:

$$C_{biotin} = \frac{n_v}{N_a} = \frac{7.5 * 10^{18}}{6 * 10^{23}} = 1.25 * 10^{-5} mol.m^{-3}$$

$$C_{biotin} \approx 10^{-5} \, mol.m^{-3} = 10^{-8} \, molar = 10 \, nmolar$$

Upper estimate:

We first estimate the concentration of biotinylated lipids in the lipid mix $C_{biotin\text{-}PEG}$. The total volume of lipid mix is V_{tot} = 50 µL, the biotinylated lipid concentration is $C_{m\ biotin\text{-}PEG}$ = 0.1 mg.mL^{-1}, the volume of biotinylated lipid is $V_{biotin\text{-}PEG}$ = 4.8 µL and the molecular weight of biotinylated lipid is $M_{biotin\text{-}PEG}$ = 3014 g.mol^{-1}. Therefore, the concentration of biotinylated lipids reads:

$$C_{biotin-PEG} = \frac{C_{m\ biotin-PEG} * V_{biotin-PEG}}{V_{tot} * M_{biotin-PEG}}$$

Given that 10 µL of lipid mix are dried and resuspended in 500 µL of internal buffer, the concentration of biotin in solution C_{biotin} is therefore:

$$C_{biotin} = \frac{C_{biotin-PEG} * 10}{500} = 6.4 * 10^{-8} \, mol.L^{-1}$$

$$C_{biotin} \approx 65 \, nmolar$$

In conclusion, the concentration of biotin sites in solution lies between 10 and 65 nM.

Intuitive understanding of the scaling behavior of spikes

The deformation of the membrane leads to a reorientation of the actin flow $\boldsymbol{\delta v} = -v_g \theta^2 \hat{\boldsymbol{z}} + v_g \theta \hat{\boldsymbol{x}}$, where $\hat{\boldsymbol{x}}$ and $\hat{\boldsymbol{z}}$ are unit vector tangent and normal to the membrane plane and $\theta \sim A/b$ is the mean membrane deflection, which decays over a distance of order b. This creates viscous stresses of order $\sigma_{zz} \sim \eta v_g \theta^2 / b \sim \eta v_g A^2 b^{-3}$ and $\sigma_{xz} \sim \eta v_g \theta / b \sim \eta v_g A b^{-2}$. Projecting these stresses along the membrane normal direction gives the same scaling as above: $\sigma_{nn} \sim \sigma_{zz} + \sigma_{xz}\theta \sim \eta A^2 b^{-3} v_g$.

Dynamics of spike growth

After 20 minutes of polymerization, spikes appear much longer than tubes, whose length is close to the thickness of the actin network (Fig. 4). Considering a well-developed spike of radius b (constant throughout spike growth – Fig. 4e) and depth A>b, the membrane area of the spike is of order $S \sim bA$, so the increase of the amount of polymerized actin inside the spike is proportional to $dV/dt \sim b\, A\, v_g$. The growth of the spike is driven by the compressive stress in the actin layer polymerizing within the spike. Assuming that the actin layer is weakly compressible, the volume inside the spike, of order Ab^2, should grow at the same rate, giving $dA/dt = v_g A/b > v_g$. This exponential growth must obviously saturate at some point due to exhaustion of the pool of actin monomer or other phenomena. However, this shows that one

generically expects spikes to grow faster than tubes, which grow at the same rate as (or slower than) the actin network growth.

Viscous model for tube initiation.

Transient physical attachments between the actin network and the membrane exist when an actin filament is bound to the activator pVCA. The bound filament being cross-linked with the rest of the growing network, it exerts an upward force (away from the membrane plane) on the membrane, and an equal and opposite downward force on the actin network. If the force on the membrnane exceeds $f_{tube} = 2\pi\sqrt{2\kappa\gamma}$, this leads to the formation of a tube. Other actin filaments bond to pVCA along the sides of the tube exerts no force in the direction of tube extension due to the fluidity of the membrane. Upon actin-pVCA unbinding at the tip of the tube, the force disappear and the tube retracts, until one of the side binding reaches the tube end, thus taking turn on the extraction force (Supplementary Fig. 11a). This effectively results in a long-lived localized force on the membrane supporting a viscous description of the actin layer (see below). In this case, the polymerization force is equivalent to a drag force proportional to the difference between the growth velocity of the actin layer and the growth velocity of the membrane tube. Using the Stokes friction force as an estimate leads to Eq.2 in the main text.

Elastic model for tube initiation, justifying a viscous description

An appropriate model for describing the mechanics of the actin network depends on the time scales of tube attachment and detachment. An elastic model is appropriate if the tube exerts a transient force on the actin network for times shorter than the viscoelastic relaxation time and if the mechanical stress in the network has time to relax while the tube is detached. A viscous model should be used otherwise, since a long-lived mechanical stress necessarily leads to actin flow at times longer than the viscoelastic relaxation time. Within a viscous model, the membrane tube effectively exerts a permanent force on the actin network (Supplementary Fig. 11a). In order to justify the viscous model we present in the main text, we present the elastic model below.

We first calculate the elastic response of the actin network to the localized force exerted by an attached membrane tube. We consider for simplicity that the network is a semi-infinite medium bounded by a flat plane (representing the liposome surface). The equilibrium equation for an infinite elastic medium with a single point-source acting on it is given by: $\Delta\vec{u} + \frac{1}{1-2\nu}\vec{\nabla}.\vec{\nabla}\vec{u} = -\frac{2(1+\nu)}{E}\vec{F}\delta(\vec{r})$, where $\nu = 0.45$ is the Poisson ratio, E the elastic modulus and $\vec{F} = (0,0,f_{tube})$ represents the vertical force exerted by the membrane tube on the network [1]. To account for the presence of the liposome membrane, we add a mirror image virtual point force that insures no net displacement of the network at the liposome surface (See Supplementary Fig. 11b for the deformation field of the network). This equation has been analytically solved, which yield a linear relation between the force and the displacement u of the network at a small distance (the mesh size ξ), away from the point force: $f_{tube} = k_p u$, where the effective network stiffness is $k_p = 2\pi\xi E/(1+\nu) \approx 10^{-4} N/m$ (with $\xi \ll h$). In our situation, the tube force is balanced by the stress exerted by the network on the liposome surface, which reads:

$$\sigma_{zz}(z=0) = \frac{f_{tube}h}{4\pi(1-\nu)}\frac{2h^2(\nu-2)+\bar{r}^2(2\nu-1)}{(h^2+\bar{r}^2)^{5/2}}$$

where $\bar{r}^2 = x^2 + y^2$ is the radius distance to the center of the tube and h the distance above the surface (length of the tube). Note that the integral of this normal stress over the lower interface balances the force exerted on the tube. The force density at the base of the tube is $\sigma_{zz}(z = \bar{r} = 0) = \frac{(2-\nu)f_{tube}}{2\pi(1-\nu)h^2}$. The force per filament at the base of the tube can now be

calculated by multiplying the force density by ξ^2, where ξ is the mesh size of the network: $f_{fil} = \sigma_{zz}(z=0)\xi^2 (\xi = 30nm$ [2]). The force per filament at the base of the tube is maximal when the tube force saturates, for a tube length $h \approx 5r_{tube} \approx 1\mu m$, where $r_{tube} = \sqrt{\kappa/(2\gamma)} \approx 140nm$ (Supplementary Fig. 11b and [3]). This force must be smaller than the actin polymerization stall force, f_{stall}, which gives the following criterion for the presence of membrane tubes within a polymerizing actin layer:

$$\gamma\xi^4 < \frac{h^4 f_{stall}^2}{2\pi^2\kappa}$$

Increasing membrane tension would eventually suppress the formation of tubes. In the accessible experimental conditions tubes are always pulled, $f_{fil} < \sigma_{zz}(z=0)\xi^2$(Fig. 5f and Supplementary Fig. 10c). Similarly, in the viscous limit, we can evaluate the viscous stress near the surface of the liposome due to the friction of the network with the tube and compare it with the polymerization stall force. By numerically evaluating this [4] we find that, since the tube is dragged along with the cortex the total force on the liposome surface does not exceed the tube extrusion force, f_{tube}~2 pN, which can be easily sustained by a small amount of filaments surrounding the tube.

Within the elastic model, we assume that the tube is bound to the actin network for an average time t_b, during which it is pulled by the growth of the network, and is detached for an average time t_{ub}, during which the tube retracts. Actin polymerization is able to drive tube formation if the net tube growth velocity, alternating phases of extraction and retraction, is positive. During the bound phase, the net displacement of the network is $v_g t_b$. The network near the attachment point with the membrane is held back by the tube force, and experiences a net displacement $u_b = v_g t_b - f_{tube}/k_p$, where $k_p \approx 10^{-4} N/m$ is the effective spring constant relating the network deformation to the localized tube force. During the phase where the membrane is unbound, the tube retracts with a velocity $v_{ub} = v_g - f_{tube}/\alpha_t$, where α_t is a friction coefficient. Using a simplified approach based on the hydrodynamics of tube extraction [5], we estimate the friction coefficient between the membrane and the network around the base of the tube $\alpha_t = 4\pi r_{tube} h \frac{\mu}{\xi^2} \approx 10^{-7} N.s/m$. Here $\mu = 10^{-6} Ns/m$ is the membrane viscosity (a crude estimate based on [5]), $r_{tube} \approx 140nm$ and evaluated at $h = 5r_{tube}$.

Defining the net average tube velocity as $\langle \dot{L} \rangle = \frac{u_b + v_{ub} t_{ub}}{(t_b + t_{ub})}$, we find: $\langle \dot{L} \rangle = v_g - \frac{f_{tube}}{k_p (t_b + t_{ub})} \left(1 + \frac{k_p t_{ub}}{\alpha_t}\right)$. We see that a positive velocity requires a long enough bound time and a short enough unbound time: typically $t_b > f_{tube}/k_p v_g \approx 10s$ and $t_{ub} < \alpha_t/k_p \approx 10^{-3} s$ (Supplementary Fig. 11d).

In the limit that $t_b \gg t_{ub}$ we obtain a relation for the critical surface tension γ and ξ to accommodate a positive velocity of the tube,

$$\gamma\xi^6 < \frac{(k_b T)^2 v_g^2 t_b^2 l_p^2}{\kappa}$$

Here we have used that $E \approx k_b T l_p/\xi^4$ [6]. Although this is only valid within the elastic description of the actin network, and is not expected to be appropriate for a permanently attached membrane tube (see main text), it predicts a critical tension for tube formation quantitatively similar to the one predicted by the viscous model. While the bound time is roughly in agreement with those reported in [7], the small value of the unbound time (corresponding to a large binding rate), can be rationalized by the fact that it does not necessarily represent the time needed for an actin filament to bind to a given pVCA molecules, but rather the time needed for actin-membrane binding site along the side of the membrane tube to reach the tip of the retracting tube where it can exert a traction force. Note that due to the fluid nature of the membrane, the attachments along the side of the tube do not

contribute significantly to the extraction force. A crude estimate for this time scale is $\alpha_t \xi / f_{tube} \approx 10^{-3} s$. This time corresponds to the characteristic time it takes to slide a distance of the mesh size along the tube, and is on the order of t_{ub}, consistent with our estimate above. The very small value of t_{ub}suggests that the tube is effectively permanently attached to the actin network during the experiment. Therefore, a viscous description of the actin layer, as presented in the main text, is more appropriate.

Membrane tube extrusion against strong turgor pressure

It was recently proven that, in budding yeast, the initiation of endocytosis relies on the growth of an Arp2/3-branched actin network [8, 9]. In this organism, high turgor pressure, in addition to membrane tension, constitutes a major obstacle to endocytosis, as it presses the membrane up against the cell wall [10]. As the actin-driven membrane tube we describe mimics membrane deformation during endocytosis, it is instructive to estimate whether the pulling force f_{drag} created by the growing actin network could lead to tube formation against a high intracellular pressure. In this case, the tube force can be written $f = \pi(\kappa/r + P\, r^2)$. The energy minimum corresponds to a tube radius $r = (\kappa/2P)^{1/3}$, yielding a tube force $f = 3\pi P\, r^2$. Equating this force with the drag force generated by the growing actin layer predicts that tube extraction is possible against intracellular pressure smaller than a threshold value $P = 2\eta v_g / r$. This remarkably simple expression gives estimates in line with more complex modeling [10, 11, 12]. Using the values corresponding to our *in-vitro* setting ($v_g = 1\ nm/s$ and $\eta = 10^4\ Pa.s$) yields a threshold pressure of order $10^3\ Pa$. On the other hand, [12, 13] using parameter values estimated for budding yeast ($v_g = 50\ nm/s$ [8] and $\eta = 2\ 10^5\ Pa.s$ [12]) yield a threshold pressure $P = 1\ MPa$, which corresponds to the turgor pressure in budding yeast [14].

References

1. Landau LD, Pitaevskii LP, Kosevich AM, Lifshitz EM. Theory of Elasticity. *123Library*, 3 edn. Butterworth-Heinemann, 2012.

2. Kawska A, Carvalho K, Manzi J, Boujemaa-Paterski R, Blanchoin L, Martiel JL, *et al.* How actin network dynamics control the onset of actin-based motility. *Proc Natl Acad Sci U S A*, **109**(36)**:** 14440-14445 (2012).

3. Derenyi I, Julicher F, Prost J. Formation and interaction of membrane tubes. *Phys Rev Lett*, **88**(23)**:** 238101 (2002).

4. Brenner H. The slow motion of a sphere through a viscous fluid towards a plane surface. *Chemical Engineering Science*, **16**(3)**:** 242-251 (1961).

5. Brochard-Wyart F, Borghi N, Cuvelier D, Nassoy P. Hydrodynamic narrowing of tubes extruded from cells. *Proc Natl Acad Sci U S A*, **103**(20)**:** 7660-7663 (2006).

6. Kroy K, Frey E. Force-Extension Relation and Plateau Modulus for Wormlike Chains. *Phys Rev Lett*, **77**(2)**:** 306-309 (1996).

7. Smith BA, Padrick SB, Doolittle LK, Daugherty-Clarke K, Correa IR, Jr., Xu MQ, *et al.* Three-color single molecule imaging shows WASP detachment from Arp2/3 complex triggers actin filament branch formation. *Elife*, **2:** e01008 (2013).

8. Kukulski W, Schorb M, Kaksonen M, Briggs JA. Plasma membrane reshaping during endocytosis is revealed by time-resolved electron tomography. *Cell*, **150**(3)**:** 508-520 (2012).

9. Picco A, Kukulski W, Manenschijn HE, Specht T, Briggs JAG, Kaksonen M. The contributions of the actin machinery to endocytic membrane bending and vesicle formation. *bioRxiv***:** (2017).

10. Dmitrieff S, Nedelec F. Membrane Mechanics of Endocytosis in Cells with Turgor. *PLoS Comput Biol*, **11**(10)**:** e1004538 (2015).

11. Zhang T, Sknepnek R, Bowick MJ, Schwarz JM. On the modeling of endocytosis in yeast. *Biophys J*, **108**(3)**:** 508-519 (2015).

12. Carlsson AE, Bayly PV. Force generation by endocytic actin patches in budding yeast. *Biophys J*, **106**(8)**:** 1596-1606 (2014).

13. Mitchison TJ, Cramer LP. Actin-based cell motility and cell locomotion. *Cell*, **84:** 371-379 (1996).

14. Minc N, Boudaoud A, Chang F. Mechanical forces of fission yeast growth. *Curr Biol*, **19**(13)**:** 1096-1101 (2009).

Supplementary Figures

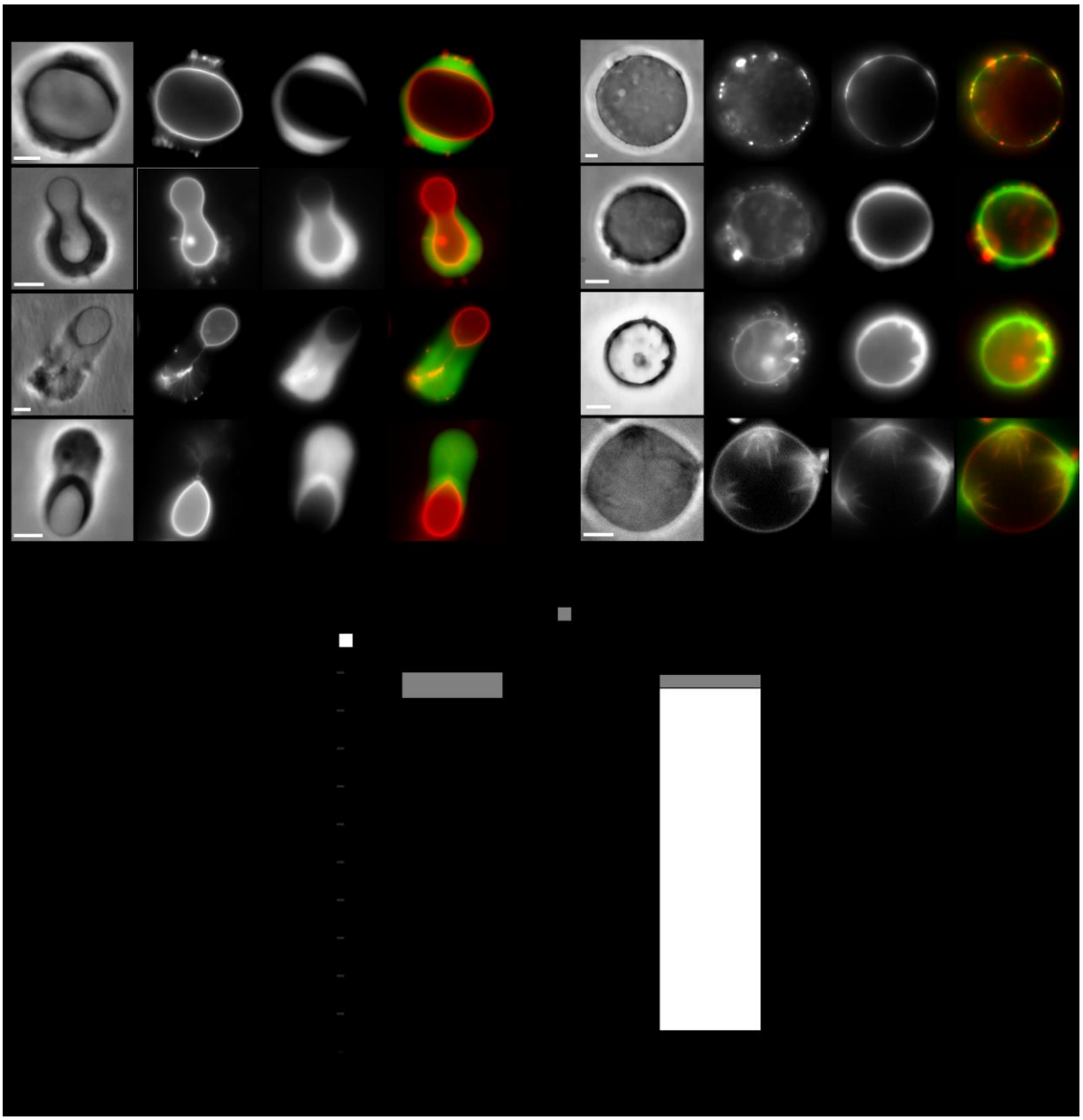

Supplementary Fig. 1: Membrane deformations in other conditions.
a, Tubes in symmetry breaking conditions. **b**, Membrane deformations in deflated conditions, quantified in Fig. 1c. (**a**, **b**) Phase contrast and epifluorescence microscopy of membrane (TexasRed-DHPE, red) and actin (Actin-Alexa Fluor 488, green). Scale bars, 5 μm. **c**, Effect of an increase in membrane tension. Number of liposomes displaying tubes, both tubes and spikes, only spikes, or undetermined. Non-deflated liposomes, n=339. Tense liposomes, n=345. All experiments in Supplementary Fig. 1c are done with the same batch of proteins, allowing for a relative comparison. Note that a different batch of proteins is used for data in Figure 1 and Supplementary Fig. 1 a and b.

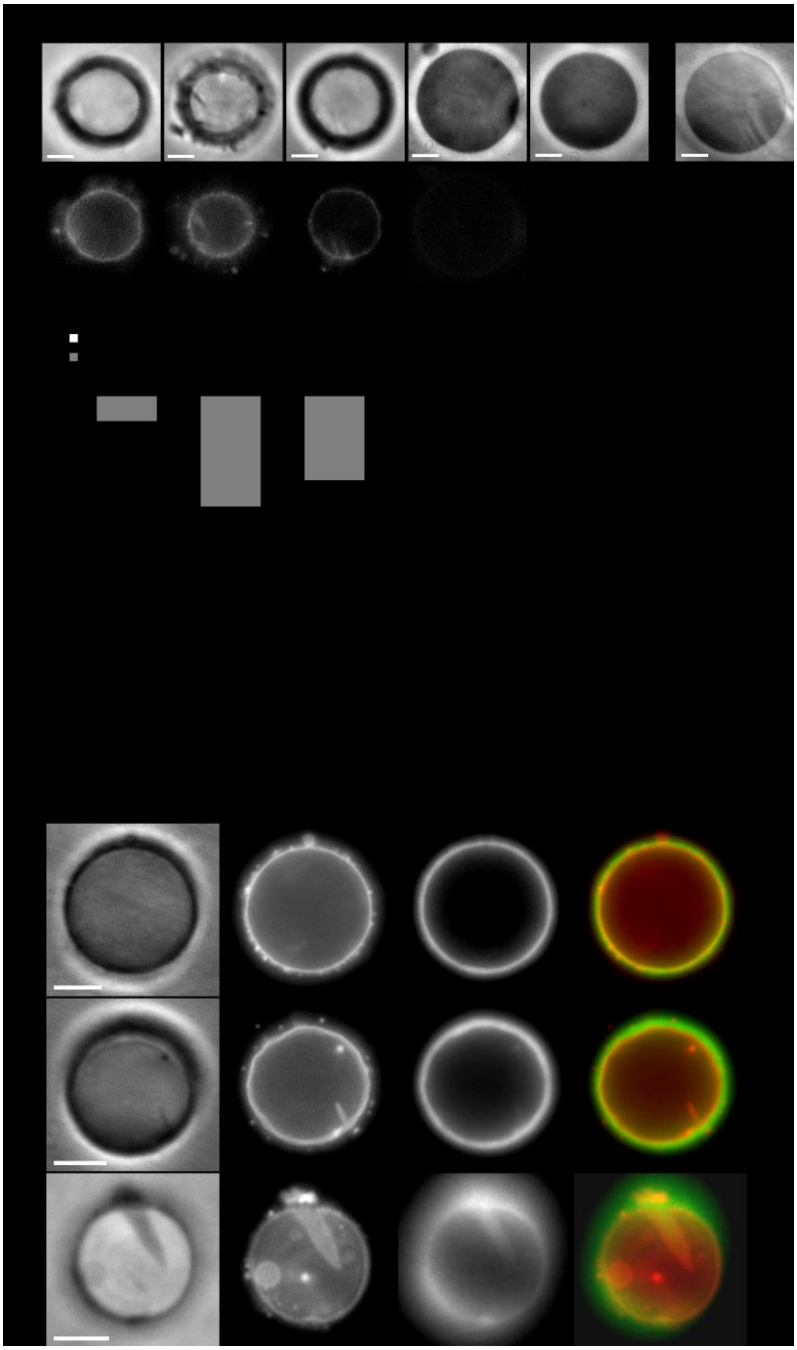

Supplementary Fig. 2: Actin polymerization with blocking biotin and with different constructs of pVCA

a, Images of liposomes developing an actin network at different biotin/S-pVCA-tetramer ratio conditions. Right, bare liposome (99.9% EPC and 0.1% biotinylated lipids) as a control. Phase contrast and epifluorescence (S-pVCA-Alexa Fluor 546). Scale bars, 5 μm. **b**, Number of liposomes displaying tubes, or both tubes and spikes, or undetermined. No biotin (n=27 liposomes from 2 experiments). Biotin at 87.5 nM (n=83 liposomes from 2 experiments). Biotin at 175 nM (n=59 liposomes from 2 experiments). Biotin at 262.5 nM (+) and 350 nM (++) display no visible actin and no visible deformation. Note that all differences are not significant except for the grey bar (tubes and spikes) between no biotin and Biotin at 87.5 nM that gives $p = 0.0137$. **c**, Phase contrast and epifluorescence images of membrane (TexasRed-DHPE, red) and actin (15% labeled Alexa Fluor 488 actin, green) for the different constructs of pVCA: S-pVCA (tetramer), GST-pVCA (dimer), pVCA (monomer). Scale bars, 5μm.

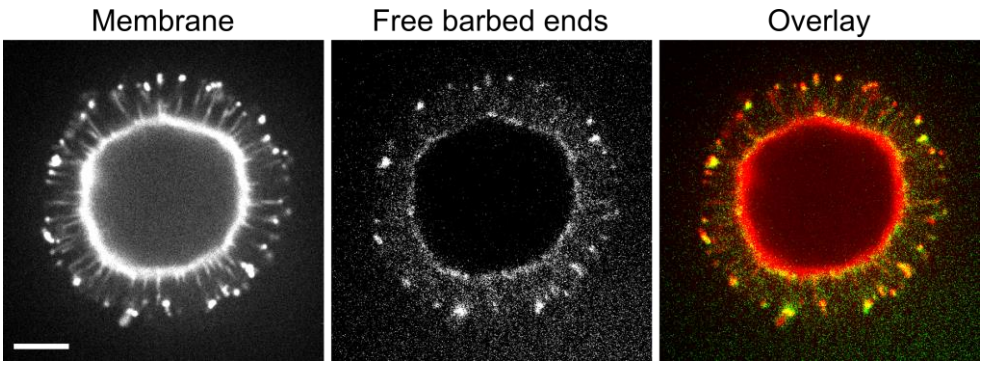

Supplementary Fig. 3: Free barbed ends within the actin network
Free barbed ends after 20 min of actin polymerization (Materials and Methods). Confocal microscopy of the membrane (TexasRed-DHPE, red) and capping proteins (Alexa Fluor 488 C_5-maleimide, green). Scale bar, 5 μm.

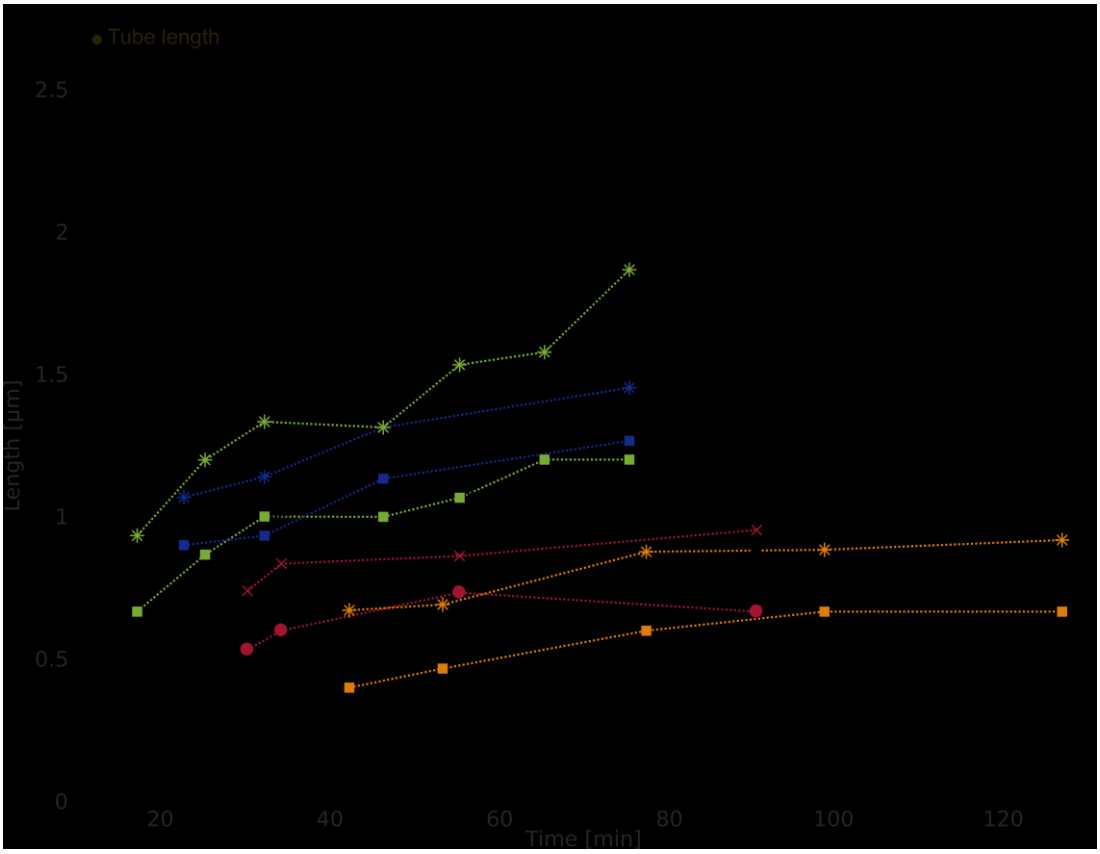

Supplementary Fig. 4: Tube and actin dynamics

Tube and actin length as a function of time. Each color represents a different tube and its corresponding actin network. Dashed lines are guides to the eye. The traces marked ** refer to the dynamics of membrane and actin corresponding to the images shown in Figure 3c.

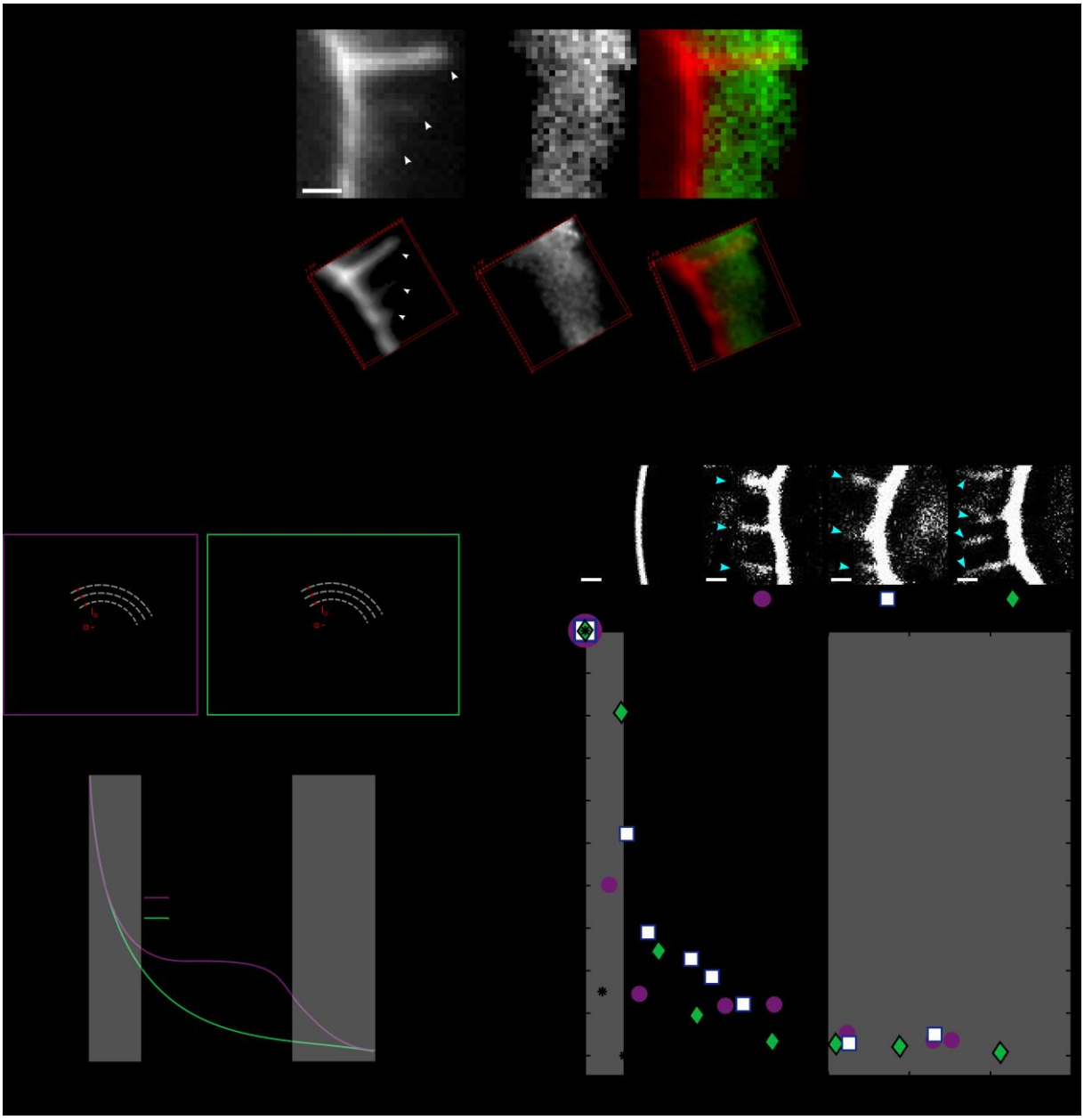

Supplementary Fig. 5: Presence of membrane tubes throughout the actin network
a, Confocal images of tubes (TexasRed-DHPE, red) within the actin network (Alexa Fluor 488, green), the tip of the tube is indicated by white arrowheads; scale bar, 1 µm. **b-c**, There is a distribution of tube lengths within the actin network, as revealed by a decrease in membrane fluorescence intensity away from the liposome surface and within the actin network thickness. **b**, Scheme describing the analysis. **c**, Top: epifluorescence images of the membrane of liposomes displaying tubes (indicated by light blue arrowheads), deconvolved from raw images by using the Gaussian blur filter from ImageJ with a radius of 7 pixels (this radius is chosen from the Gaussian curve of the bare membrane); scale bars, 5 µm; bottom: fluorescence intensity normalized by $I_{tot}(r_1)$, each symbol represents the analysis of the corresponding top image above.

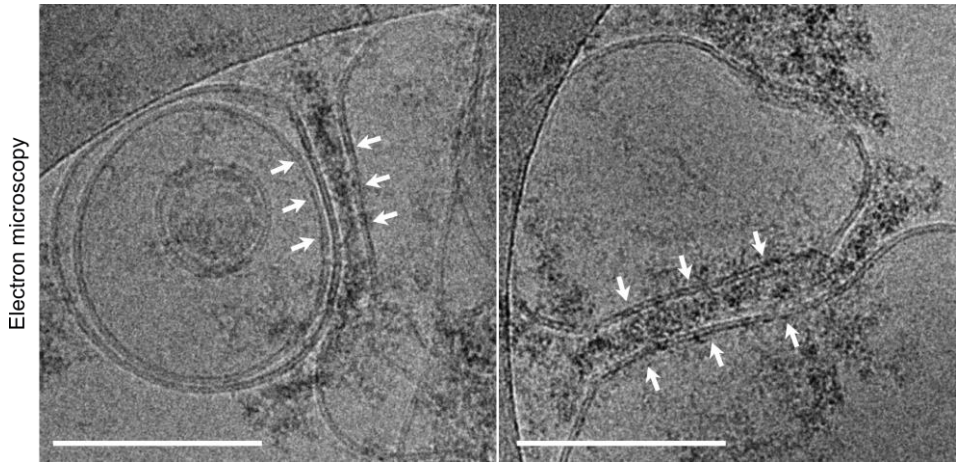

Supplementary Fig. 6: Electron microscopy
Cryo-electron microscopy images of small liposomes (99.9% EPC, 0.1% biotinylated lipids) incubated with S-pVCA (350 nM) for 15 min prior to freezing. White arrows point where membranes are flattened by sticking together with protein aggregates. Scale bars, 100 nm.

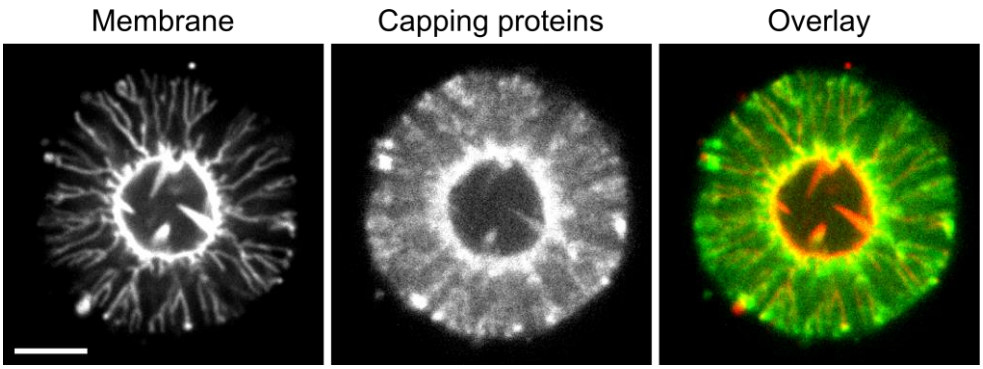

Supplementary Fig. 7: Capping proteins fill in spikes
Confocal microscopy of membrane (TexasRed-DHPE, red) and capping proteins (Alexa Fluor 488 C_5-maleimide, green). Scale bar, 5 μm.

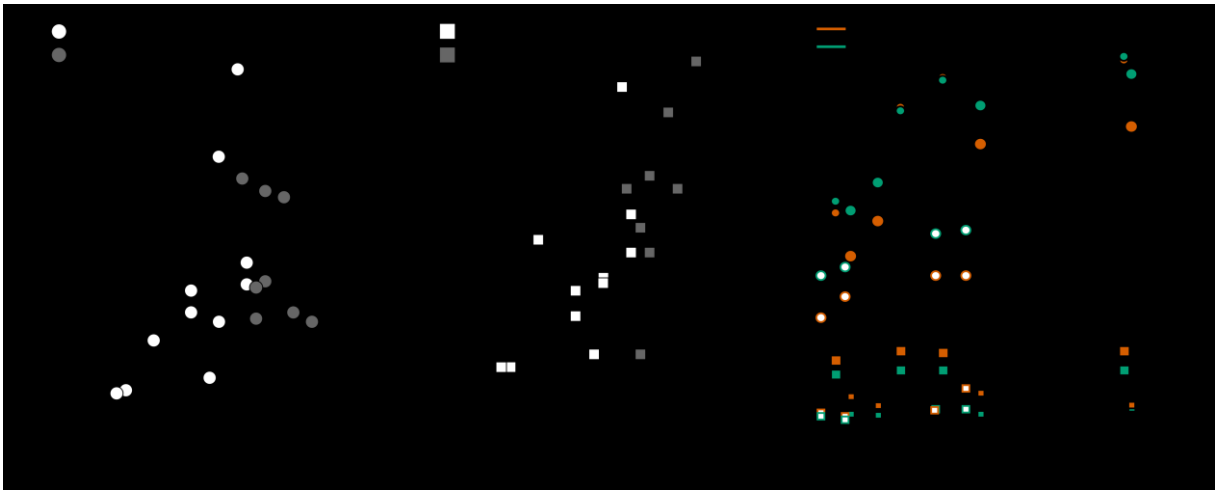

Supplementary Fig. 8: Spike dependence of actin network thickness at its base, in non-deflated or deflated liposome condition

a, Spike length as a function of actin network thickness next to its base. **b**, Spike width at the base of the spike as a function of actin thickness next to its base. Dashed line corresponds to a linear fit of slope 1. **c**, Evolution of spike length and width over time. Dashed lines are guides for the eyes. Circles: spike length; Squares: spike width. Each layout refers to one spike. The traces marked * refer to the dynamics of membrane and actin corresponding to the images shown in Figure 4c.

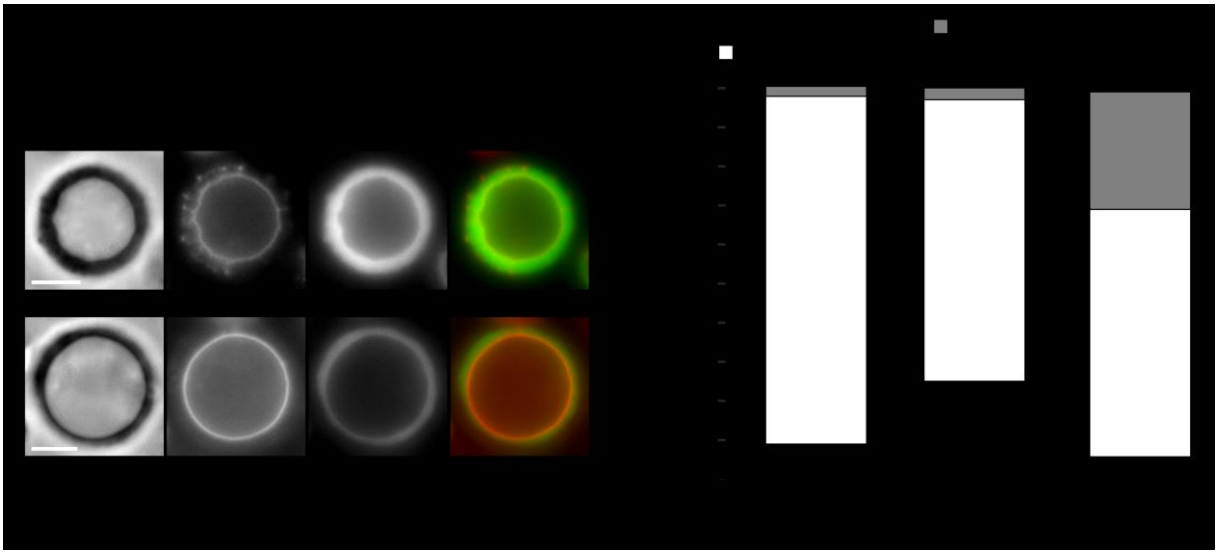

Supplementary Fig. 9: Effect of tension and network architecture on membrane deformations

a, Phase contrast and epifluorescence images of liposomes with a loosened but visible actin network, displaying tubes or not; non-deflated conditions. **b**, Effect of actin network architecture on both non-deflated and deflated liposomes. Number of liposomes displaying tubes, both tubes and spikes, only spikes, or undetermined. Non-deflated liposomes, reference condition, n=281 from 3 experiments. Non-deflated liposomes, loosened network, n=668 from 4 experiments. Deflated liposomes, loosened network, n=241 from 2 experiments.

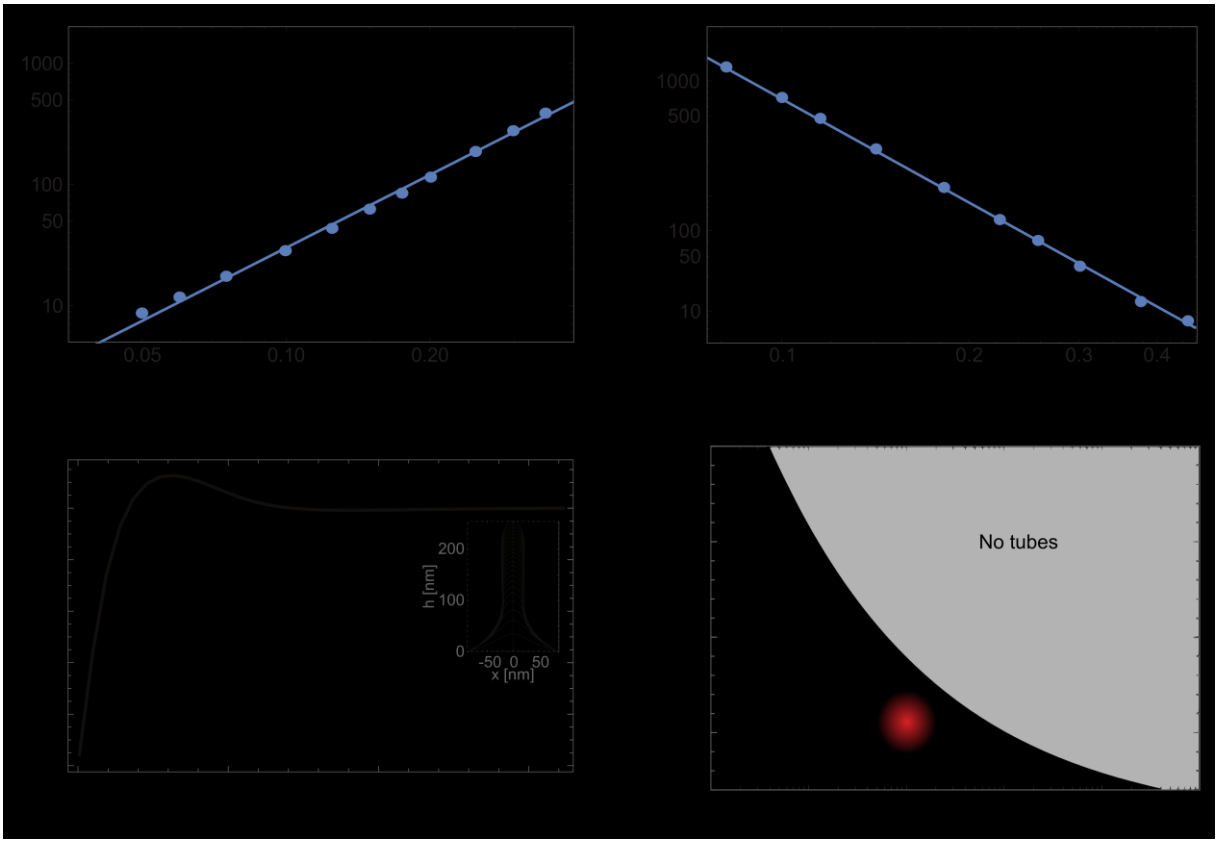

Supplementary Fig. 10: Additional theoretical results for spike initiation and tube formation

a-b, Spikes: Scaling of the normal stress σ_{nn} created by an actin network growing on a deformed surface as function of the deformation amplitude *A* for a value of its width $b = 0.22\ \mu m$ (**a**) and as a function of the width for a value of $A = 0.15\ \mu m$ (**b**) ($v_g = 1$ *nm/s*, viscosity $\eta = 10^4$ *Pa.s*). These results are consistent with the scaling given in the text: $\sigma_{nn} \sim \eta A^2 b^{-3} v_g$. **c**, Dimensionless force required to pull a membrane tube, applying a point force at the tip of the membrane as function of the length of the tube. **d**, Phase diagram derived from Eq. 2, as a function of mesh size ξ and membrane tension γ. Grey part, region where the viscous driving force is not sufficient to extract a tube ($f_{tube} = 2\ pN$, $\kappa = 10kT$ and $h = 100\ nm$). Red point, experimental reference condition.

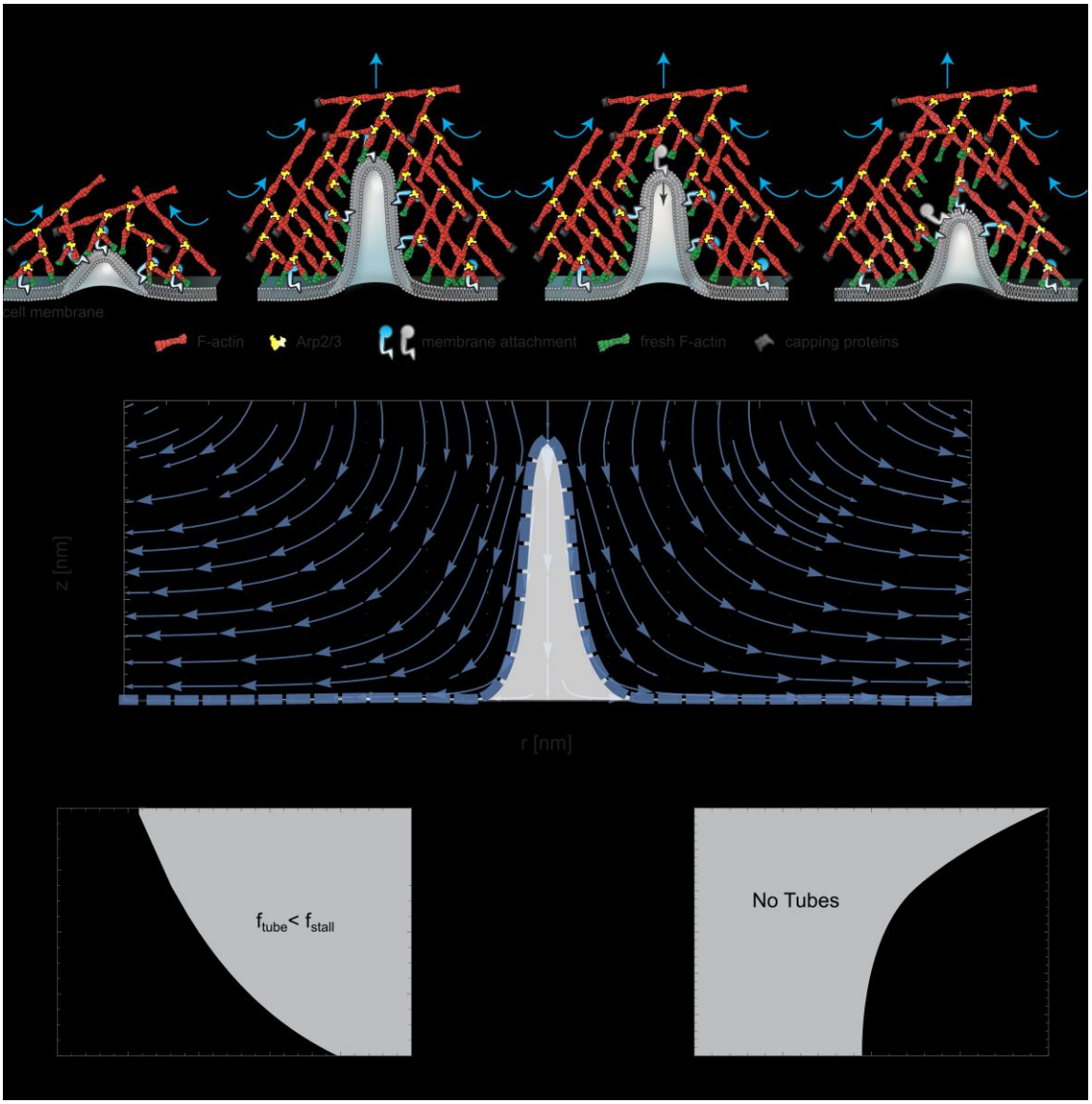

Supplementary Fig. 11: Elastic model for tube formation
a, Scheme of a membrane tube pulled by the actin network and retraction due to detachment. Blue arrows indicate forces within the actin network. **b**, Deformation field for a point force applied inside an elastic material (actin network) near a solid wall, as a function of the distance relative to the center of the tube. **c**, Phase diagram for the mechanics of tube pulling as a function of the mesh size ξ and the membrane tension γ. The grey part represents the region where the stall force around the tube is reached and no tube can be pulled. The white region corresponds to forces per filament below the stall force, and a tube can be pulled. **d**, Phase diagram for the kinetics of tube pulling as a function of t_b and t_{ub} that are respectively the bound and unbound times and where $\alpha_t = 10^{-7}N.\frac{s}{m}$, $k_p = \frac{100pN}{\mu m}$ and $f_{tube} = 2pN$. The white region corresponds to a situation where a tube is pulled, the grey region to a situation where no tube is pulled. The line corresponds to a typical value of $v_g = 1\frac{nm}{s}$.